PHYSICAL REVIEW MATERIALS **4**, 033405 (2020)

Thermal conductivity and its relation to atomic structure for symmetrical tilt grain boundaries in silicon

J. Hickman[1] and Y. Mishin[2]

[1]*Materials Science and Engineering Division, National Institute of Standards and Technology, Gaithersburg, Maryland 20899-8910, USA*
[2]*Department of Physics and Astronomy, MSN 3F3, George Mason University, Fairfax, Virginia 22030, USA*

(Received 16 December 2019; accepted 12 March 2020; published 30 March 2020)

We perform a systematic study of thermal resistance and conductance of tilt grain boundaries (GBs) in Si using classical molecular dynamics. The GBs studied are naturally divided into three groups according to the structural units forming the GB core. We find that, within each group, the GB thermal conductivity strongly correlates with the excess GB energy. All three groups predict nearly the same GB conductivity extrapolated to the high-energy limit. This limiting value is close to the thermal conductivity of amorphous Si, suggesting similar heat transport mechanisms. While the lattice thermal conductivity decreases with temperature, the GB conductivity slightly increases. However, at high temperatures it turns over and starts decreasing if the GB structure undergoes a premelting transformation. Analysis of vibrational spectra of GBs resolved along different directions sheds light on the mechanisms of their thermal resistance. The existence of alternating tensile and compressive atomic environments in the GB core gives rise to localized vibrational modes, frequency gaps creating acoustic mismatch with lattice phonons, and anharmonic vibrations of loosely bound atoms residing in open atomic environments.

DOI: 10.1103/PhysRevMaterials.4.033405

I. INTRODUCTION

Thermal conductivity of dielectric materials plays an important role in many technological applications [1–8]. In nano- and microelectronic devices, it is often desirable to have a high thermal conductivity in order to quickly remove the Joule heat from critical components. On the other hand, thermoelectric efficiency of energy conversion devices can be improved by increasing the thermal resistance of the material without (or with as small as possible) reduction in the electric carrier mobility.

In dielectric materials, the thermal conductivity is primarily due to atomic vibrations, by contrast to metals where the electronic mechanism dominates. It is well established that the thermal resistance of semiconductor materials can be increased by creating a high density of internal interfaces, such as grain boundaries (GBs) and heterojunctions [1,3–12]. This approach is especially efficient in thin films, where the film surfaces serve as additional interfaces for phonon scattering. While high-frequency phonons scatter primarily at point defects (such as vacancies and dopant atoms), it is the low-frequency (long-wavelength) acoustic phonons that are scattered most effectively by interfaces. To be able to control the thermal resistance of materials, it is important to understand the microscopic mechanisms involved in the phonon scattering at interfaces. This work is focused on thermal resistance of GBs, which is often referred to as the GB Kapitza resistance.

The nature of phonon scattering at GBs is poorly understood, especially with respect to the relationship between the GB structure and the thermal resistance. It is recognized that a GB is not simply a barrier that can either reflect or transmit phonons, but a layer of matter that has its own structure, vibrational modes, and thus mechanisms of heat transport. Unfortunately, experiments do not provide information detailed enough to understand the role of the GB structure. The existing theories, such as the acoustic mismatch model (AMM) [13] and the diffuse mismatch model (DMM) [9] capture the physics of the two materials but not of the interface [14]. Both usually disagree with experiment on a quantitative level. For symmetrical GBs, the AMM is not even applicable because the grains have the same acoustic properties and the model predicts perfect transmission. The DMM treats GBs as structurally amorphous, and even then, works only for high-frequency phonons [14]. Furthermore, it has been argued that phonon scattering by interfaces cannot be properly described using only the vibrational modes that exist in the two bulk materials separated by the interface [15]. Simulations based on the Boltzmann transport equation [16] and other continuum approaches do not capture the role of the GB structure either. At best, an average/effective thermal resistance of GBs in a polycrystalline sample can be treated in the effective medium approximation [17].

At present, classical molecular dynamics (MD) simulations offer the most effective way to establish the link between the bicrystallography and atomic structure of GBs, on one hand, and the GB thermal resistance, on the other [14,18–27]. Specifically for Si GBs, which are the subject of this paper, the previous MD studies were focused on twist GBs [14,19,20,25,28,29] and were not very systematic. Tilt boundaries were recently studied in SiC [30]. For pure silicon, however, we are aware of only two MD studies. One was conducted by Maiti *et al.* [18] for [001] symmetrical tilt $\Sigma 5$ and $\Sigma 13$ boundaries (Σ being the reciprocal density of coincident sites in the coincident site lattice theory [31]). In the second, Chen *et al.* [23] investigated the heat resistance of three [011] symmetrical tilt GBs ($\Sigma3$, $\Sigma9$, and $\Sigma19$) by heat pulse propagation from a point source.

It should be noted that all previous studies of Si GBs utilized the interatomic potential developed by Stillinger and Weber (SW) [32]. As any interatomic potential, the SW potential has its strengths and weaknesses, which were discussed in detail in the recent literature [33,34]. While it reproduces the lattice thermal conductivity reasonably well, its ability to predict the correct GB structures is questionable. For this reason, in this work we chose to use the recently developed generalized and optimized Tersoff-type potential [33], which we consider more reliable for the modeling of Si GB structures.

The goal of this work was to conduct a systematic atomistic simulation study of thermal resistance of Si GBs with the intention of (1) establishing the structure–thermal resistance relationships and (2) better understanding the impact of the GB structure on the phonon scattering. After introducing our simulation methodology in Secs. II and III, we present the equilibrium structures of a large set of [001] symmetrical tilt GBs with misorientation angles spanning the entire range of symmetrically distinct bicrystallographies (Sec. IV A). We prefer to work with tilt GBs, rather than twist, because their structures are generally simpler and experimental data are available for comparison. By comparing the GB structures, energies, free volumes, and other properties over a wide range of temperatures up to the melting point, we find that all GBs studied here naturally break into three categories or groups. These groups are characterized by different combinations of properties and distinct structural units forming the GB core. We also find that some of the boundaries remain structurally ordered up to the melting point, while others develop a significant degree of structural disorder due to the premelting effect. In Sec. IV B, we report on the calculated thermal resistance and conductance of the GBs, showing that the three structural groups mentioned above follow three different types of correlation among the GB conductance, the GB thermal width, and the GB energy. The thermal conductance also correlates with the GB disorder, showing a marked dip at high temperatures when the structure begins to premelt. To gain insights into the physical mechanisms behind the structure-conductance relationships, we compare the thermal conductivities and local vibrational spectra of the GB core regions with those of crystalline, amorphous and liquid Si at different temperatures (Sec. IV C). In Sec. V, we summarize our findings, point to unresolved problems, and discuss possible future directions.

II. METHODS OF THERMAL CONDUCTIVITY CALCULATIONS

Two most common methods for computing the phononic thermal conductivity of bulk phases via molecular dynamics (MD) simulations are the nonequilibrium MD (NEMD) and the Green-Kubo (GK) method. Both methods have been previously applied to Si using different interatomic potentials [35–39]. In the NEMD approach, a fixed temperature differential is created across the material, which generates a heat flux $\boldsymbol{J}$. This flux and the temperature T initially vary in time and space. After the steady state is reached, both $\boldsymbol{J}$ and the temperature gradient ∇T become constant in time and uniform across the system. In the small ∇T limit, the heat transport follows the Fourier law

$$\boldsymbol{J} = -\kappa \nabla T, \tag{1}$$

where κ is the thermal conductivity and $\rho = 1/\kappa$ is the thermal resistivity of the material (both are scalars for an isotropic material). Alternatively, a constant heat flux can be imposed in the simulations, giving rise to a steady-state temperature gradient. In either case, κ can be extracted from Eq. (1) using the steady-state values of $\boldsymbol{J}$ and ∇T. Variations of the NEMD method include the approach to equilibrium method [40] and its sinusoidal version [41].

The GK formalism [42,43] tracks equilibrium fluctuations of the heat flux to compute the ensemble-averaged heat current autocorrelation function (HCACF) $\langle \boldsymbol{J}(0) \cdot \boldsymbol{J}(t) \rangle$ as a function of time t. The method is based on the fluctuation-dissipation theorem [44] and expresses the thermal conductivity as the integral

$$\kappa = \frac{V}{3k_B T^2} \int_0^\infty \langle \boldsymbol{J}(0) \cdot \boldsymbol{J}(t) \rangle dt, \tag{2}$$

where V is the system volume and k_B is Boltzmann's constant. This method is only applied to homogenous systems and cannot be utilized to study GB phonon scattering.

Among other approaches, the phononic Boltzmann transport equation can be solved in the mode-specific relaxation time approximation [38,39,45]. This method combines lattice dynamics or classical MD to compute the phonon relaxation times with quantum-mechanical treatment of the heat capacity. In addition to being applicable to temperatures below the experimental Debye temperature, this methods has certain computational advantages over the NEMD and GK approaches and is capable of providing more detailed information about the physics of phonon scattering. It has recently been applied to Si [38,39] in conjunction with the Tersoff [46,47] and environment-dependent interatomic potentials (EDIP) [48]. *Ab initio* methods have also been used to extract the thermal conductivity [49–52].

Heat transport across interfaces is best modeled by the NEMD method. Suppose the material contains a planar interface of width w whose normal vector points in the heat flux direction y. The steady-state temperature profile $T(y)$ across the material is expected to be linear in the bulk regions on either side of the interface. However, the interface usually acts as a thermal resistor to the heat flux, causing a sharp increase in the temperature gradient within the interface region. On the length scale much larger than w, the temperature profile appears to be discontinuous at the interface [14,18]. By Fourier's law, the magnitude of the temperature discontinuity (jump) ΔT is proportional to the heat flux through the interface:

$$J = \sigma_K \Delta T = \frac{\kappa_K}{w} \Delta T. \tag{3}$$

Here, σ_K is the Kapitza conductance of the interface, $R_K = 1/\sigma_K$ is the Kapitza resistance, and κ_K is the average Kapitza conductivity in the interface region. (The Kapitza resistance was first discovered in 1941 by Peter Kapitza while studying the superfluidity of helium [53,54].) Knowing J and ΔT, Eq. (3) can be used to extract the Kapitza conductance. The average interface conductivity can be then evaluated using a reasonable estimate of the interface width w. This NEMD approach will be applied in this work.

Phonon scattering by interfaces has also been studied by simulating incident wave packets representing phonons [14]. Examining the packet scattering process it is possible to compute the energy transmission coefficient as a function of phonon frequency, which provides information about the ability of different boundaries to inhibit the propagation of different types of phonon. While the wave-packet simulations can provide physical insights as well as input data to other models, extracting the Kapitza conductance directly from the simulations is extremely challenging. Another approach to studying the boundary scattering is offered by the coherent phonon pulse method [55–57], in which a heat pulse generates a flux of coherent and diffuse phonons scattered by GBs. This method leverages the regular MD by introducing the concurrent atomistic-continuum approach [56]. The latter gives access to larger length scales and thus helps overcome the wavelength truncation effect arising in regular MD simulations due to the small computational model size. The method was successfully applied to study the GB Kapitza resistance in Si [23] and a two-dimensional (2D) Lennard-Jones material [22]. These studies have demonstrated the roles of the phonon frequency, ballistic or diffusive character, GB structure, and other factors in the boundary resistance to heat fluxes. Despite the advantages in gaining a more detailed understanding of the scattering process, this method is not designed to deliver precise values of the Kapitza resistance.

III. SIMULATION METHODOLOGY

A. Computational methods

Atomic interactions in Si were modeled using an optimized Tersoff-type potential [33] that was fitted to both experimental and first-principles data. The potential accurately predicts many Si properties, including the elastic constants, the phonon density of states, point defects, surfaces, and many other properties. The melting temperature predicted by the potential is 1687 K, which perfectly matches the experimental value. This potential will be denoted throughout this work as MOD2. For comparison, some of the simulations were repeated with other potentials as will be discussed later. The software package LAMMPS (Large-Scale Atomic/Molecular Massively Parallel Simulator) [58] was utilized for both 0 K structural minimization and MD simulations at finite temperatures. We used some of the built-in commands of LAMMPS, including the commands for computing the radial distribution function, the heat flux $\boldsymbol{J}$, the velocity autocorrelation function, the bond-order parameter Q_6, and on-the-fly binning and averaging of the simulation results. Visualization and structural analysis were performed with the OVITO software package [59].

Unless otherwise stated, all simulations used periodic boundary conditions in all three directions and a 1-fs integration time step. For simulation blocks containing a GB, such boundary conditions imply the existence of two GBs in each block. To achieve a physically accurate mechanical state during equilibrium GB simulations, we enforce a fixed cross-sectional area in the plane of the GB with zero stress in the GB normal direction. To this end, we utilize a variant of the NPT ensemble, which we denote NP_yT. In this ensemble, the system temperature is regulated by a thermostat and the dimensions of the simulation block in the x and z dimensions are held constant (constant GB cross-sectional area), while the y dimension (normal to the GB) is allowed to vary to ensure a zero y component of stress ($P_y = 0$). Most of the simulations were performed for crystalline Si with the diamond cubic structure. This crystalline structure will be referred to as c-Si, or simply Si if no confusion can arise. Before carrying out the c-Si simulations at elevated temperatures, the temperature dependence of the equilibrium lattice constant was computed by stress-free NPT MD simulations at temperatures ranging from 100 K up to the melting point at 50-K increments. To eliminate thermal stresses in the lattice during MD simulations, the lattice was pre-expanded to the equilibrium lattice constant at the respective temperature prior to the simulation. This was done for all simulation runs that utilizes the NVT, NP_yT, or NVE ensembles.

B. Structure generation

1. Grain boundary structures

To conduct a systematic study of the effect of misorientation angle on the GB thermal conduction, it was necessary to prepare a set of equilibrium GB structures by carefully minimizing their energies. We chose to focus on the $(hk0)[001]$ family of symmetrical tilt GBs, where [001] is the tilt axis and $(hk0)$ is the GB plane. For such boundaries, the tilt angle θ is given by $\theta = 2\tan^{-1}(k/h)$ and the reciprocal density of coincident lattice sites Σ is obtained from the relations $h^2 + k^2 = \Sigma$ or $h^2 + k^2 = 2\Sigma$ [31]. The 31 tilt angles studied in this work covered the entire interval $0^\circ \leqslant \theta \leqslant 90^\circ$ of symmetrically distinct misorientations. Since the tilt axis is fixed and the boundaries are symmetrical, we can refer to them by the Miller indices of the respective GB plane. For example, the $\Sigma5(210)[001]$ ($\theta = 53.1^\circ$) GB can be referred to as simply (210) boundary. For clarity, we emphasize the difference between the misorientation angle θ used in the present work and the disorientation angle $\tilde{\theta}$, which is often used in the GB literature. For the simple class of [001] tilt GBs, the disorientation angle can easily be recovered from θ by $\tilde{\theta} = \theta$ for $\theta \leqslant 45^\circ$ and $\tilde{\theta} = 90^\circ - \theta$ for $45^\circ < \theta \leqslant 90^\circ$. The coordinate axes x, y, and z were aligned along the $[k\bar{h}0]$, $[hk0]$, and [001] crystallographic directions, respectively. Thus, the y direction was normal to the GB plane and the z direction was parallel to the tilt axis. The dimensions of the simulation block varied according to the type of simulation, as will be detailed below.

The GBs were created by standard geometric constructions in which the lattice was aligned relative to the coordinate system according to the crystallographic orientation of the lower grain ($y < 0$), followed by 180° rotation of the upper half of the block ($y > 0$) around the y axis. To equilibrate the GB structure, multiple rigid translations parallel to the GB plane were applied to one of the grains and the total energy was minimized with respect to atomic displacements by the conjugate gradient method. The GB structure with the smallest excess energy γ was taken as closest to equilibrium.

In some cases, the translations were followed by heating the system to a high temperature and briefly annealing it before the conjugate gradient minimization. The anneal temperature and time were typically 1500 K and 25 ps, respectively, but could vary from one GB to another in search of the lowest energy.

It has recently been demonstrated that adding or removing atoms to or from the GB region can reveal new structures with even lower energies than those obtained by closed-system simulations [60–66]. Motivated by these findings, we applied the atomic removal methodology developed in our recent work [66] to a subset of the Si GBs. The method computes the GB energy as a function of the fraction λ of atoms removed from the GB core. The function $\gamma(\lambda)$ obtained can have local minima corresponding to stable or metastable GB structures. The method is computationally expensive and could only be implemented for a limited number of boundaries.

2. Liquid and amorphous structures

Liquid and amorphous Si structures, referred to as l-Si and a-Si, respectively, were included for comparison with GBs. The l-Si structure was generated by carrying out a 20-ps NPT MD run at 3000 K starting from c-Si, which produced a fully melted structure. This structure was then equilibrated by longer NPT MD runs at several different temperatures, before performing production runs to determine the thermal conductivity at respective temperatures.

To obtain a-Si structure, an l-Si sample was cooled down by a 500-ps NPT MD run in which the temperature was decreased from 3000 to 300 K as a linear function of time. This run was short enough to avoid recrystallization but long enough to allow for some local atomic relaxation. The structure obtained was further annealed in the NPT ensemble for 2 ns at 300 K to allow for additional atomic relaxation. This structure was used as the starting point for the subsequent simulations at several other temperatures. At each chosen temperature, the equilibrium volume was determined by a stress-free NPT simulation, followed by a production run in the NVT ensemble at the equilibrium volume. To demonstrate that the amorphous structure was stable, the mean square displacement (MSD) of atoms was determined during the simulations. At temperatures below 500 K, the MSD was found to be small and time independent, showing that long-range atomic diffusion was negligible. Above 500 K, MSD began to increase as a linear function of time, signaling the onset of atomic diffusion. Based on this observation, the thermal conductivity of a-Si was only computed below 500 K when the heat transport could be cleanly separated from mass transport.

C. The structural disorder quantification

To quantify the emergence of structural disorder in some of the GBs at high temperatures, the Q_l order parameters introduced by Steinhardt *et al.* [67] were computed as functions of temperature. Specifically, it was found that the single parameter Q_6 was sufficient for our purposes, being close to zero inside the grains and positive in the GB. For computational reasons, the block sizes for the disorder quantification runs were approximately $3.5 \times 10 \times 3.5\,\text{nm}$ with periodic boundary conditions in all dimensions. This block size was sufficient for calculating the local structure within the core regions of the various GBs, but is significantly smaller than the simulation blocks used in the thermal conductivity calculations. At each temperature, the two GBs in the simulation block were equilibrated by the usual procedures described above and subject to a 12-ns-long MD run using the NP_yT ensemble. During the run, approximately 3000 snapshots containing atomic positions and Q_6 parameters of atoms were saved at regular time intervals. At the postprocessing stage, the order parameter profile $Q_6(y)$ was computer for each snapshot by averaging over bins parallel to a given GB. The peak arising at the GB was fitted by a Gaussian function and the Q_6 value averaged over a 0.5-nm window at the center of the Gaussian was taken as the GB order parameter. Such values were averaged across the snapshots to obtain the order parameter of the GB. These order parameters were analyzed as functions of temperature as will be discussed below. During the Q_6 calculations, the mean-square atomic displacements within the GB cores were also computed to determine whether atomic diffusion was occurring.

D. Nonequilibrium molecular dynamics simulations

The NEMD simulations utilized the approach [37,68,69] in which a chosen heat flux was imposed across the GB and the temperature jump ΔT was measured after the steady state regime was confirmed. Prior to the simulation, the system, which was periodic in all dimensions, was pre-expanded according to the desired average temperature and thermalized by running MD in the NP_yT ensemble for 100 ps. The MD ensemble was then switched to NP_yH (fixed enthalpy and constant cross-sectional area defined by the x and z directions), so as to continue enforcing $P_y = 0$ while allowing for a nonequilibrium temperature distribution in the simulation block.

The heat flux normal to the GB was imposed by introducing hot and cold slabs (thermostats) parallel to the GB plane and artificially transferring a fixed increment of kinetic energy, $2\delta K$, between them by rescaling the atomic velocities at each time step Δt of the MD simulation. The number of atoms in the two slabs was equal to ensure that the energy exchanges were symmetric. These artificial exchanges of kinetic energy resulted in a physical heat flux from the hot slab to the cold with the magnitude $J = \delta K / A \Delta t$, where A is the GB area. In simulations with the average temperature below 1000 K, a $J = 25\ \text{GW m}^{-2}$ flux was imposed, which is comparable to fluxes commonly reported in the literature [14,29]. In simulations above 1000 K, a flux of $J = 50\ \text{GW m}^{-2}$ was applied, which is somewhat larger than in previous work. This increase in the flux was required to resolve the temperature jump, which at high temperatures tended to be small. As a consistency check, the actual flux was independently computed using the heat flux function built into LAMMPS, and the results were found to be in excellent agreement with the flux predicted from the kinetic energy transfers.

The temperature profile $T(y, t)$ was computed by averaging the local kinetic energy of atoms over an appropriate timescale and relating it to temperature through the equipartition theorem. (It should be noted that care is needed when

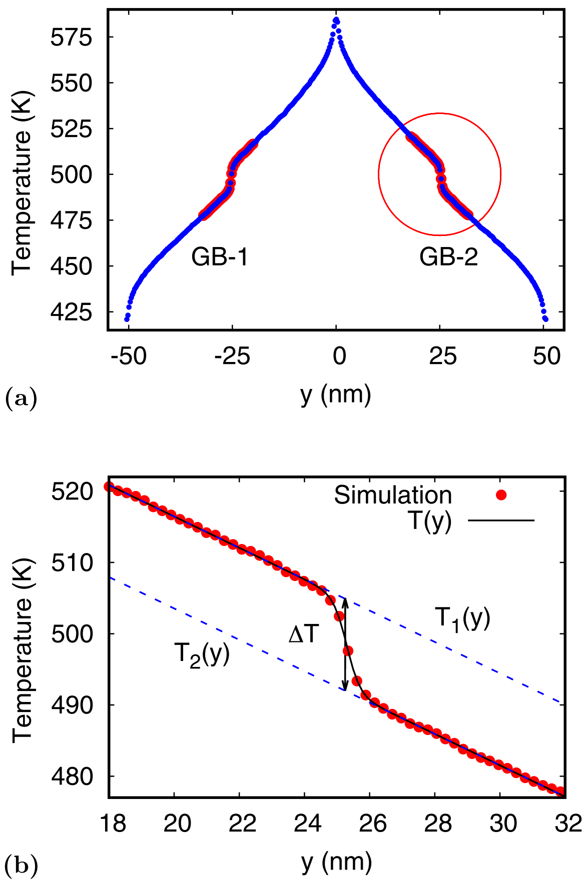

FIG. 1. (a) Typical temperature profile for the (210) GB with the mean temperature of 500 K. The hot and cold thermostats are located at $y = 0$ and $y = \pm 50$ nm, respectively. GB-1 and GB-2 are two GBs existing in the simulation block due to periodic boundary conditions. (b) Enlargement of the encircled region showing the procedure for computing the temperature jump ΔT. The black line is the fit by Eq. (4). The blue lines are the linear portions of the fitted function given by Eqs. (6) and (7).

defining temperature in this way, especially when dealing with short time intervals in which the concept of "instantaneous" temperature becomes ill defined [70,71].) This calculation utilized LAMMPS' internal commands to partition the simulation block into narrow bins parallel to the GB and average the local temperatures inside the bins to produce a smooth temperature curve. Before carrying out the production runs, the local temperatures were allowed to reach the steady state by running NEMD for 1 ns. The production run was 4 ns long and produced a time-averaged temperature profile $T(y)$ used to extract σ_K. To this end, the temperature profile was fitted by the function

$$T_{\pm}(y) = -\frac{J}{\kappa}(y - y_0) \mp \frac{\Delta T}{2} \tanh\left(\frac{y - y_0}{2w}\right) + T_0, \qquad (4)$$

where the two sign choices reflect the fact that the simulation block has two GBs exposed to heat flowing in opposite directions (Fig. 1). Here, κ is the bulk thermal conductivity, y_0 is the location of the center of the GB, T_0 is the local temperature at the GB location (which is close to the average temperature in the simulation block), ΔT is the temperature jump, and w controls the width of the hyperbolic tangent and has the meaning of the thermal width of the GB. The flux J is known. The remaining variables κ, y_0, T_0, ΔT, and w were treated as fitting parameter and were determined by minimizing the mean-square deviation of the actual temperature profile from Eq. (4). This fit did not include the nonlinear regions close to the thermostats where the temperature profile was distorted by boundary effects. An example of the fit is shown in Fig. 1. An advantage of this method is that the single fit allows us to extract the temperature jump required for computing the Kapitza conductance σ_K, the GB width w that can be used to evaluate the GB conductivity

$$\kappa_K = \sigma_K w, \qquad (5)$$

and the lattice thermal conductivity κ. In the limits of $y \gg y_0$ and $y \ll y_0$, Eq. (4) reduces to two linear functions offset from each other by ΔT,

$$T_1(y) = \left[-\frac{J}{\kappa}(y - y_0) + T_0\right] + \frac{\Delta T}{2} \qquad (6)$$

and

$$T_2(y) = \left[-\frac{J}{\kappa}(y - y_0) + T_0\right] - \frac{\Delta T}{2}. \qquad (7)$$

These functions represent the steady-state temperature profiles inside the grain on either side of GB-2 (Fig. 1). Their slopes give the temperature gradients in the grains and thus $-J/\kappa$. The values of σ_K and κ obtained from the fit were further averaged over the two GBs present in the simulation block due to periodic boundary conditions. At temperatures above 750 K when thermal fluctuations were large, the calculation was repeated several times starting from different initial conditions and the results were averaged.

To verify the system-size convergence of the NEMD Kapitza conduction results, we varied the GB area and the length of the simulation block in the y directions using the $\Sigma5[210]$ GB as a test case. Previous studies have indicated that the converged dimensions depend on the interatomic potential [36,38,72,73]. For the present interatomic potential, it was found that the system dimensions of roughly $4.4 \times 100 \times 5$ nm ensured reasonably converged Kapitza conductance values. Details of the convergence tests can be found in the Supplemental Material [74].

E. The Green Kubo method

To demonstrate the consistency of the simulation methodology, κ was also computed at several temperatures for c-Si, l-Si, and a-Si samples using equilibrium MD and the GK relation (2). The simulation block was pre-expanded according to the equilibrium volume at the chosen temperature and thermally equilibrated by an NVT run for 100 ps. A 10-ns-long production run was carried out in the microcanonical (NVE) ensemble to compute the HCACF $\langle \boldsymbol{J}(0) \cdot \boldsymbol{J}(t) \rangle$. The entire MD time was partitioned into intervals of length τ and the product $\boldsymbol{J}(t_i) \cdot \boldsymbol{J}(t_i + t)$ was averaged over all atoms and all MD integration points t_i within each interval to obtain the HCACF. Examples of the HCACF's obtained in this work are shown in Fig. 2.

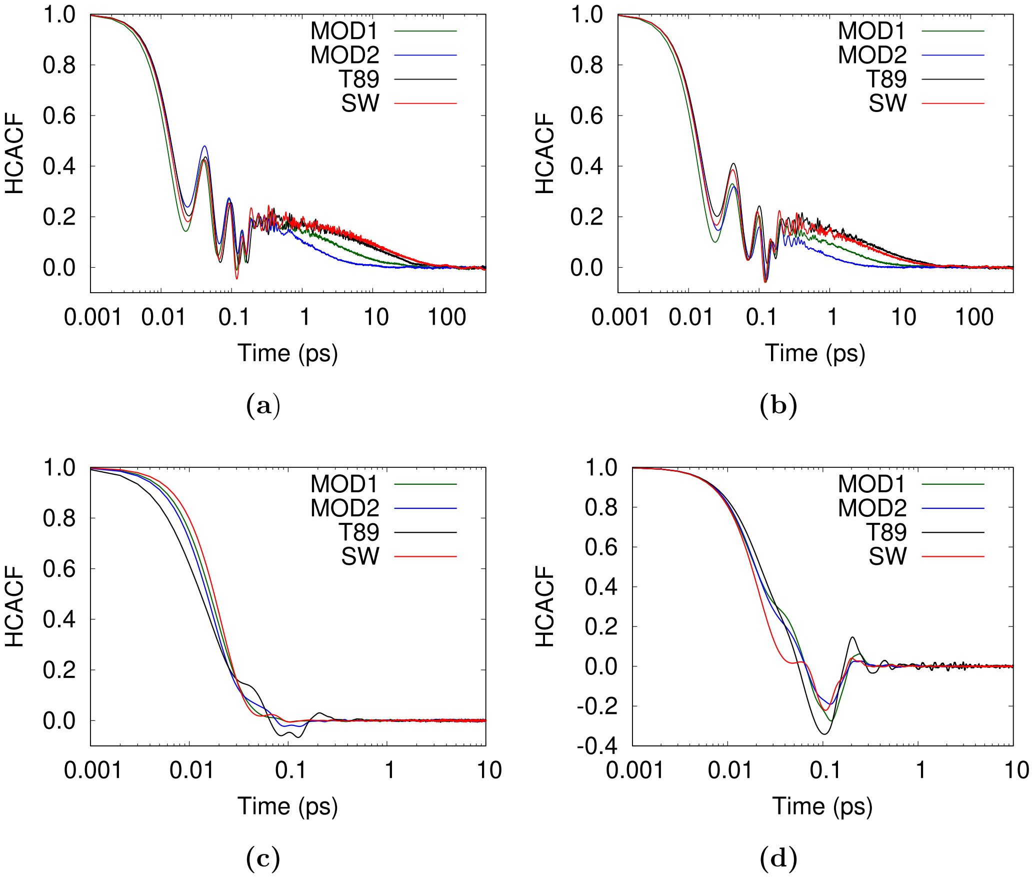

(a) (b) (c) (d)

FIG. 2. The HCACF computed for c-Si using four interatomic potentials at 500 K (a) and 1000 K (b), for l-Si at 2000 K (c), and for a-Si at 300 K (d). Note the difference in the timescales between panels (a) and (b) and panels (c) and (d). The potentials tested: SW [32], T89 [75], MOD1 [76], and MOD2 [33].

To obtain the thermal conductivity from Eq.(2), the HCACF was numerically integrated from zero to τ. The choice of the correlation time τ is an important step in the procedure and is known to affect the accuracy of the results [36,38,39,72,73]. It should be emphasized that this time depends on the interatomic potential used. To put our results in perspective with the literature, the calculations were repeated with several alternate potentials. For the SW [32] and 1989 Tersoff (T89) [75] potentials, the correlation time in c-Si was found to be on the order of 100 ps [38,39,72,73]. With the MOD2 potential [33], τ was significantly shorter, approximately 8 to 12 ps, depending on the temperature (Fig. 2). The MOD1 potential [76] presented an intermediate case. To assert the convergence with respect to τ, the thermal conductivity as a function of τ and extrapolated to infinity by fitting it with the function $\kappa(\tau) = \kappa_\infty \tanh(\tau - \tau_0)$, τ_0, and κ_∞ (extrapolated value of κ) being the fitting parameters. A typical example of fitting is shown in Fig. 3. For l-Si and a-Si, the correlation time was relatively short (1 to 5 ps) and the converged values were readily obtained by setting $\tau = 10$ ps. Convergence with respect to the system size was also investigated and the results were in excellent agreement with the literature [35,38,39,73]. It was found that the system dimensions of 6.5 × 6.5 × 6.5 nm (13 824 atoms) were sufficient for obtaining well-converged conductivity values.

Table I summarizes the thermal conductivity values at representative temperatures computed in this work with four different interatomic potentials. (It should be mentioned that the l-Si and a-Si structures were prepared with the MOD2 potential and were rescaled to the new equilibrium volumes

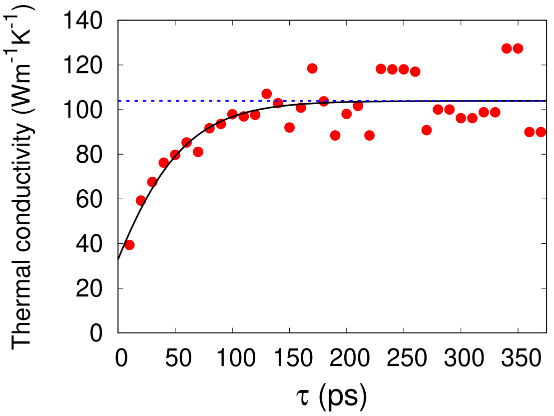

FIG. 3. Thermal conductivity computed using the GK method with the T89 potential [75] plotted as a function of the upper integration limit τ. The solid line is a fit with the function $\kappa(\tau) = \kappa_\infty \tanh(\tau - \tau_0)$ discussed in the text. The dashed blue line indicates the converged value.

TABLE I. Comparison of thermal conductivities (in W m^{-1} K^{-1}) computed with four interatomic potentials for c-Si, l-Si, and a-Si at different temperatures. The potentials tested were SW [32], T89 [75], MOD1 [76] and MOD2 [33]. T_m is the melting temperature computed with the respective potential.

	c-Si		l-Si	a-Si	T_m
	500 K	1000 K	2000 K	300K	K
MOD1	28.6	14.7	0.7	0.84	1682[d]
MOD2	13.0	5.4	1.0	1.1	1687[d]
SW	157.4	43.5	1.4	1.2	1677[d]
T89	103.5	58.7	1.1	1.6	
Experiment	75.2[a]	25.1[a]	*	1.8[b], 1.1[c]	1687[d]

[a] Predicted from the polynomial fit κ^{-1} [W^{-1} mK] $= 1.33 \times 10^{-5}T + 2.66 \times 10^{-8}T^2$ to experimental data for ^{28}Si [77].

[b] Reference [78].

[c] Reference [79].

[d] Reference [33].

* Comparison is meaningless because thermal conductivity of liquid Si is dominated by the electronic contribution [80].

when switching to other potentials.) Predictions of the SW and T89 potentials overestimate the experimental data, whereas the MOD1 and especially MOD2 potentials significantly underpredict the experiment. The reasons for choosing the MOD2 potential for this work over other existing potentials was mentioned in Sec. I and will be discussed again in Sec. V. For a-Si, all four potentials predict very similar values in good agreement with experiment. While experimental data for l-Si is available [80], comparison with classical MD simulations has little significance since the heat transport in l-Si is dominated by the electronic contribution. It should be noted, however, that the four potentials predict similar values of κ_l on the order of 1 W mK^{-1}.

F. The vibrational density of states

Vibrational spectra of various atomic environments were computed using the velocity autocorrelation function (VACF) method [81]. One advantage of this method is that it can be applied to selected atomic groups or even an individual atom. The VACF of an atom is defined by

$$C_v(t) = \frac{\langle \mathbf{v}(0) \cdot \mathbf{v}(t) \rangle}{\langle \mathbf{v}(0) \cdot \mathbf{v}(0) \rangle}, \tag{8}$$

where $\mathbf{v}(t)$ is the atom's velocity. In practice, the ensemble average $\langle \ldots \rangle$ is replaced by averaging over multiple initial conditions $\mathbf{v}(0)$ and across atoms with identical local environments. In anisotropic environments, it is useful to examine the VACF projected along specific directions. For example, the VACF projected along the Cartesian axis x is defined by

$$C_{v_x}(t) = \frac{\langle v_x(0) \cdot v_x(t) \rangle}{\langle v_x(0) \cdot v_x(0) \rangle}, \tag{9}$$

and similarly for the $C_{v_y}(t)$ and $C_{v_z}(t)$ projections. The vibrational density of states (DOS) $g(\omega)$ is obtained by taking the Fourier transform of $C_v(t)$. The projected DOS $g_x(\omega)$ is defined as the Fourier transform of $C_{v_x}(t)$ [accordingly, of $C_{v_y}(t)$ and $C_{v_z}(t)$ for $g_y(\omega)$ and $g_z(\omega)$].

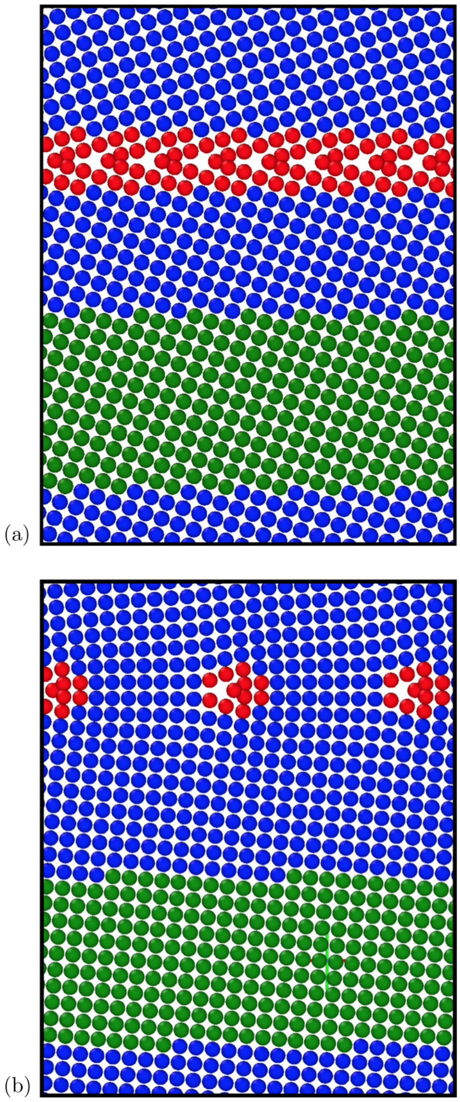

FIG. 4. Groups of atoms selected for the calculation of local vibrational DOS of crystalline lattice (green) and GB atoms (red) in the (a) (210) GB and (b) (650) GB. The GB plane is horizontal and the tilt axis is normal to the page.

For l-Si and a-Si, only $C_v(t)$ and $g(\omega)$ were computed. The averaging in Eq. (8) was performed over all atoms in the simulation block. The time averaging was performed by repeating a 15-ps-long NVE MD simulation 25 times starting from different initial conditions (15 ps exceeds the correlation time). The averaged VACF was then transformed to the frequency domain.

To probe the dynamic properties of GBs, their density of states (DOS) was computed for atoms within the cores of the (210) and (650) GBs at the temperatures of 300 and 1600 K. To gather better statistics, the simulation blocks constructed for the Kapitza conductance calculations (see above) were replicated several times in x and z dimensions. The c-Si lattice DOS was computed from about 200 000 atoms residing in a region chosen inside one of the grains as shown in green

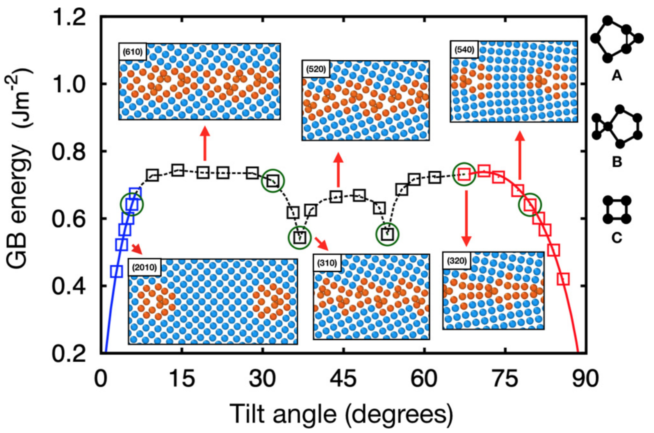

FIG. 5. GB energy γ as a function of tilt angle θ. The inset figures represent typical GB structures with fundamental structural units A, B, and C shown on the right. The structures are projected along the [001] tilt axis normal to the page. The blue atoms have a diamond-like local environment whereas the orange atoms have local environments deviated from diamond. The square symbols represent the GBs used for the systematic study of Kapitza conductance at the fixed temperature of 750 K. The green circles represent GBs selected for a less systematic study at different temperatures. The color of the squares reflects the different structural categories discussed in the text. The solid red and blue lines were obtained by Read-Shockley fits [83]. The dashed black lines serve as a guide for the eye.

in Fig. 4. The lattice DOS was validated by independent calculations based on the dynamical matrix method [82] and excellent agreement was obtained. For the GBs, the VACF was averaged over around 50 000 atoms identified as belonging to the GB core using the excess energy criterion. In Fig. 4, such atoms are shown in red. They form a continuous layer in the high-angle (210) GB and decorate individual dislocation cores in the low-angle (650) GB. The projected VACF in all three coordinate directions was computed to differentiate between vibrational effects in the GB normal direction and in the GB plane directions. It should be noted that, in the highly nonhomogeneous structure of a GB, each atoms has its own distinct density of states. Thus, the GB DOSs characterize averaged dynamical properties of all atoms residing in the GB core. The local DOSs of individual GB atoms can differ from each other very significantly. To probe this difference, we calculated DOS for several representative atomic sites chosen within the GB core. The results will be discussed below.

IV. RESULTS

A. Grain boundary structures

Figure 5 shows the GB energy γ as a function of the tilt angle θ, along with several representative GB structures and the fundamental structural units found in this work and in the previous literature [84,85]. A complete catalog of the GB structures obtained in this work can be found in the Supplemental Material [74].

The shape of the energy-angle curve is qualitatively similar to the one reported previously [84–87]. Most of the GB structures are also in good agreement with literature reports when available [84–86,88,89]. The (320) and (310) GB structures are additionally consistent with the high-resolution electron microscopy observations [90]. One discrepancy with the literature is our structure of the (510) boundary. This boundary has been extensively studied and at least twelve different structures have been reported [84,88]. In Ref. [88], our lowest-energy structure of this boundary [74] was found to have the second lowest energy out of eight structures tested. This minor difference is likely to be related to the different interatomic potentials used in the two studies. The agreement between the simulated and experimentally known structures gives us confidence that other predicted GB structures are also reliable.

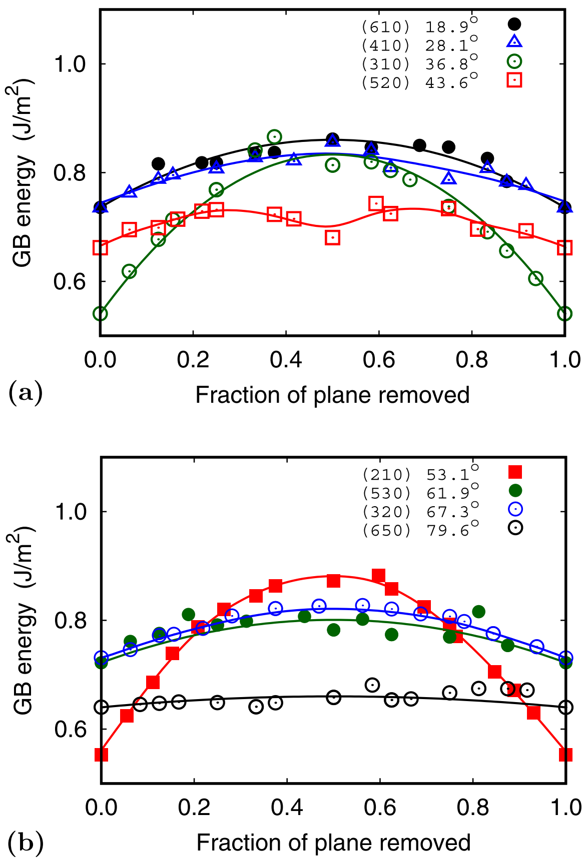

FIG. 6. Energy of selected GBs as a function of the number λ of atoms removed from the GB (fraction of atomic plane). (a) Tilt angle $\theta \leqslant 43.6^\circ$. (b) Tilt angle $\theta \geqslant 53.1^\circ$. The lines are drawn to guide the eye.

As mentioned in Sec. III B 1, some of the GBs were additionally equilibrated by varying the atomic density λ in the GB core using the methodology developed in Ref. [66]. By contrast to metallic GBs, where variations in λ revealed new stable or metastable structures (GB phases) [60–64,66], no new structures were found in the Si GBs whose energies would be lower than those obtained by the standard method ($\lambda = 0$). Figure 6 shows GB energy versus λ plots for a set of GBs tested by this method. In all cases, the energy has a single minimum at $\lambda = 0$ (and $\lambda = 1$ by periodicity), showing that there are no additional GB phases present. The only exception is the (520) boundary, which has a local minimum at $\lambda = 0.5$ corresponding to a metastable GB phase. For all other values of λ, this GB represents distorted, vacancy-riddled forms of the lowest-energy structure obtained at $\lambda = 0$.

By examining all GB structures and energies obtained in this work, it was found that they could be divided into three groups. Group 1 includes low-angle GBs with $\theta \lesssim 7^\circ$. Such boundaries are composed of A-type structural units (Fig. 5) forming the cores of the edge dislocations separated by elastically distorted lattice regions. An example of group 1 structures is given by the (20 1 0) boundary with $\theta = 5.73^\circ$ shown in Fig. 5. Group 2 is more inclusive and encompasses the GBs over the angular range $7^\circ \lesssim \theta \lesssim 65^\circ$. They are characterized by densely packed structural units with little or no lattice gaps between them. The structural units are mostly B type arranged in linear or zigzag patterns. Examples are given by the (610), (310), and (520) GBs shown in Fig. 5. Finally, the GBs assigned to group 3 have the tilt angles in the range $65^\circ \lesssim \theta \lesssim 90^\circ$ (i.e., disorientation $0^\circ \lesssim \tilde{\theta} \lesssim 25^\circ$). They are composed of discrete dislocations whose cores are formed of B-type structural units separated by lattice regions. It should be noted that the choice of the bounding angles between the groups is somewhat subjective, but it is consistent with the natural grouping of the GBs according to their Kapitza conductance, as will be discussed below.

The foregoing discussion was focused on GB structures at zero temperature. To evaluate the temperature effect, a set of representative GBs was selected to examine their structural evolution with increasing temperature. For some of them, such as the (310) and (210) GBs, the atomic structure remained practically unchanged up to temperatures close to the melting point, except for thermal displacements of atoms from the average positions. Other GBs developed a significant atomic disorder at high temperatures. The disordering of core regions of crystalline defects at high temperatures falls in the category of premelting phenomena, which for metallic GBs have been thoroughly studied by theoretical models and atomistic simulations [91–93]. A similar GB disordering at high temperatures was previously observed in Si, specifically in the $\Sigma25(710)$ tilt boundary [94] and several twist boundaries [95]. In this work, this effect has been demonstrated for a larger set of tilt GBs, including low-angle boundaries such as (20 1 0) 5.73° and (650) 79.6°. The latter case is illustrated in Fig. 7 for the (650) GB whose structure is composed of discrete dislocations running parallel to the tilt axis and normal to the page. As temperature increases, the dislocation cores become increasingly disordered and eventually turn into liquid pipes at temperatures approaching the melting point (1687 K).

To quantitatively demonstrate the accumulation of disorder in the GBs, the order parameter Q_6 was computed as discussed in Sec. III C. The results obtained for a set of six GBs are summarized in Fig. 8. The order parameters in the crystalline and liquid phases of Si are shown for comparison. As expected, the order parameter in the GBs is lower than in the perfect crystal but higher than in the liquid. In the (310) and (210) GBs, the order parameter decreases linearly with temperature with approximately the same rate as in c-Si [Fig. 8(a)]. This behavior is consistent with the fact the structure of these boundaries is preserved at all temperatures. The decrease in their order parameter is solely due to the increased amplitude of atomic vibrations. In the remaining GBs [Fig. 8(b)], the order parameter decreases linearly at low temperatures but deviates down from this trend at temperatures above 1250 K. This deviation signals the onset of additional disordering, which becomes especially pronounced near the meting point. This accelerated disordering reflects the GB premelting behavior affecting these boundaries.

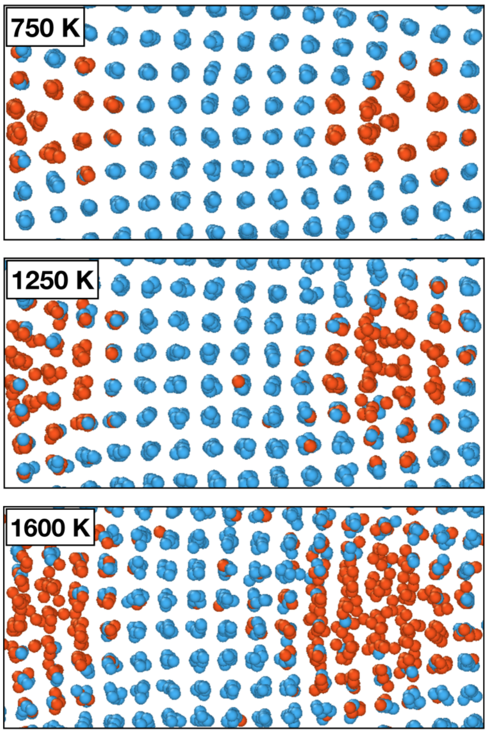

FIG. 7. Atomic structure of the (650) GB at different temperatures. The atoms with diamond-like local environment are shown in blue, while atoms with distorted environments are shown in orange. Note the high level of disordering in the dislocation cores forming the boundary at the highest temperature (1600 K).

B. Grain boundary thermal conductance

1. Simulation details

A typical steady-state temperature profile $T(y)$ obtained by NEMD simulations is shown in Fig. 1. The profile consists of linear segments inside the grains and a temperature jump ΔT arising at the GB due to its Kapitza resistance. The nonlinear regions near the hot and cold thermostats are caused by increased phonon scattering and were commonly observed in previous studies [14,18,27]. In the present simulations, the temperature difference between the thermostats was around 150 K at low temperatures and as high as several hundred Kelvin at high temperatures. The values of ΔT were typically around 10 to 20 K.

To demonstrate the robustness of our simulation methodology and insensitivity of the main conclusions with respect to the choice of the interatomic potential, the Kapitza conductance of three GBs was computed at 500 and 1000 K using four different potentials. The results were compared with literature data when available. The $\Sigma5(210)$ and $\Sigma5(310)$ GB structures were created with the MOD2 potential and scaled according to the thermal expansion coefficients of other

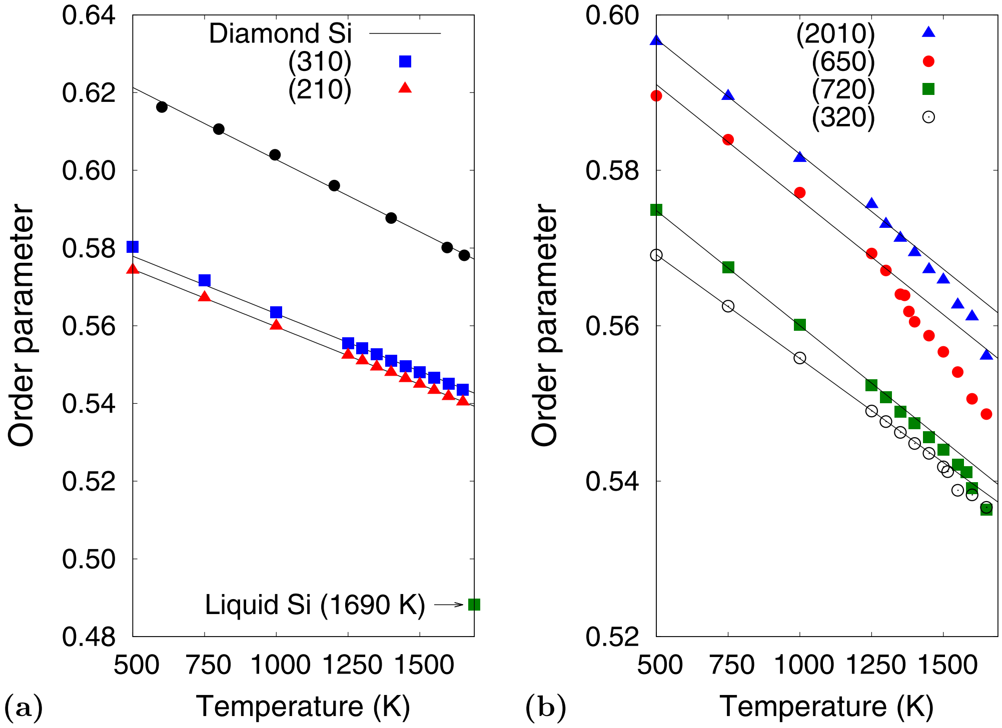

FIG. 8. The GB order parameter as a function of temperature. (a) (310) and (210) GBs show a linear decrease in the order parameter due to atomic vibrations. (b) GBs show an accelerated decrease of order at high temperatures approaching the melting point (1687 K) caused by premelting. The order parameters in c-Si and l-Si (at 1690 K) are shown for comparison.

potentials. For the $\Sigma5(310)$ GB, a metastable structure was used to facilitate comparison with previous calculations [14]. The $\Sigma101(10\,1\,0)\,11.42^\circ$ twist boundary was equilibrated with the SW potential [32] to ensure full consistency with the previous work [14]. The 0 K energy of this boundary was found to be 0.91 J m^{-2}, which is exactly the number reported in Ref. [14]. The results are summarized in Table II. The Kapitza conductance obtained in this work compares well with the previous reports [14,18] and shows relatively small variations across the four potentials. The latter observation is in contrast with the results for the lattice thermal conductivity of c-Si, which was shown to be much more sensitive to the choice of the potential (Table I).

2. Tilt angle dependence

We will first present the results obtained by fixing the average temperature at 750 K and studying a set of GBs over the entire range of tilt angles. The goal was to elucidate the effects of GB energy, GB structure, and the lattice misorientation on the Kapitza conductance. The temperature of 750 K is above the experimental Debye temperature of Si (658 K [96]) but low enough that even the lowest-angle GBs produced a temperature jump that could be reliably determined to extract the Kapitza conductance.

As an example, Fig. 9(a) presents a collection of temperature profiles for several low-angle (relative to a misorientation of 90°) GBs. Note that the lowest-angle GB has a very small temperature jump due to its relatively large conductance σ_K, and that generally ΔT grows (σ_K decreases) as the tilt angle deviates down from 90° (increased disorientation $\tilde{\theta}$). Figure 9(b) summarizes the conductance of all GBs studied in this work plotted as a function of the GB energy γ. An important observation is that the results fall into three categories distinguished by different colors. These categories correspond to the three structural groups discussed in Sec. IV A, specifically

TABLE II. Thermal conductance σ_K of selected GBs (in GW $\mathrm{m}^{-2}\,\mathrm{K}^{-1}$) computed with different interatomic potentials. The results are compared with literature data when available [14,18]. The potentials tested: SW [32], T89 [75], MOD1 [76], and MOD2 [33].

	$\Sigma5(310)[001]$ tilt		$\Sigma5(210)[001]$ tilt		$\Sigma101(10\,1\,0)$ twist	
	500 K	1000 K	500 K	1000 K	500 K	1000 K
MOD1	1.25	1.92	1.54	2.10	1.58	2.03
MOD2	1.36	1.97	1.94	2.47	1.65	2.03
SW	1.21, 0.9[a]	1.80	1.38	1.94	1.53, 1.63 ± 0.2[b]	1.92, 1.95[b]
T89	1.41	2.03	1.71	2.14	1.66	2.43

[a] Reference [18].
[b] Reference [14].

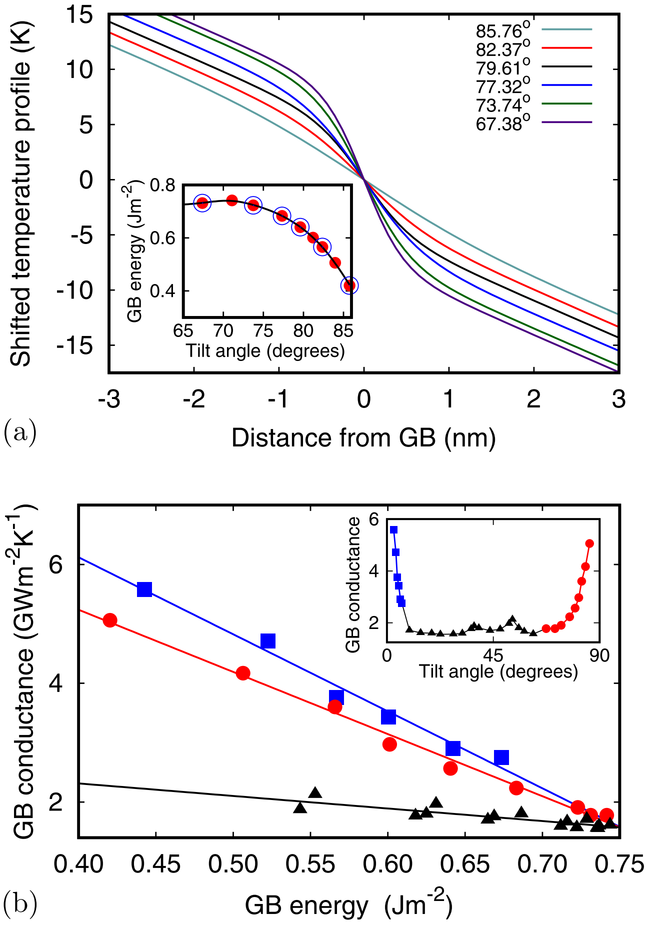

FIG. 9. (a) Temperature profiles for low-angle (relative to 90°) GBs at 750 K. The profiles were fitted by Eq. (4) and shifted to zero by subtracting the average temperature of the simulation block. (b) Kapitza conductance of all GBs studied in this work as a function of GB energy at 750 K. Note that the results naturally break into three groups as discussed in the text. The lines represent linear fits intended to highlight the trends. The inlays show the plots of the GB conductance σ_K versus the tilt angle.

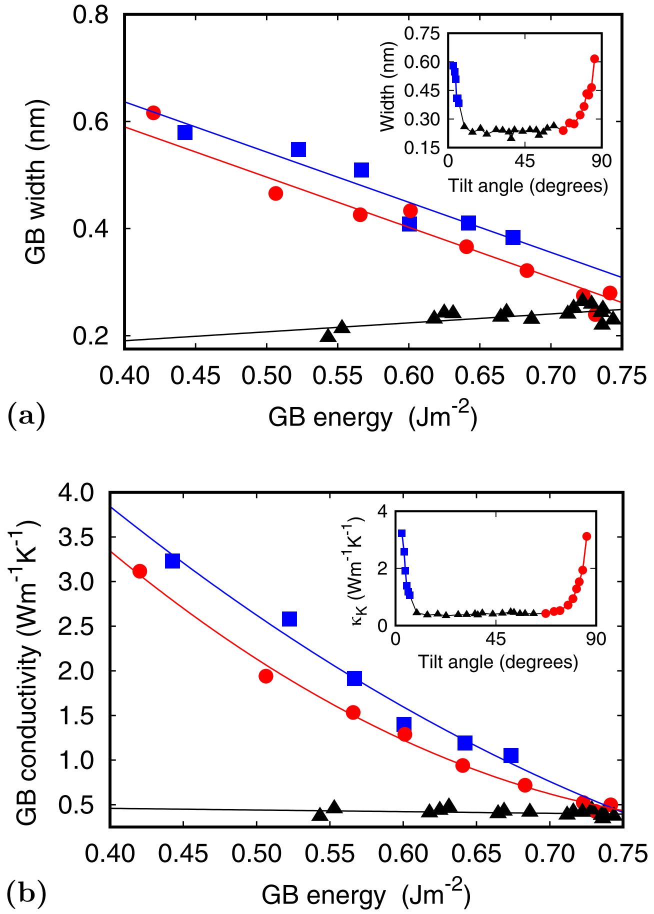

FIG. 10. Thermal width w (a) and GB conductivity κ_K (b) as functions GB energy at 750 K. The lines are drawn to highlight the trends. The inlays show the plots of w and κ_K versus the tilt angle.

group 1 (blue), group 2 (black), and group 3 (red). Within each group, the conductance follows a linear dependence on γ. The linear correlation lines are shifted relative to each other and have different slopes. A similar trend was previously observed for Si twist boundaries [19] as well as symmetric tilt GBs in MgO [97]. The low-angle GBs of group 1 have the highest conductance and are closely followed by Group 3 GBs. The Group 2 GBs with intermediate tilt angles have the lowest conductance. It is interesting to note that in all three groups, σ_K approaches the same, universal value of approximately $1.75\,\mathrm{GW\,m^{-2}\,K^{-1}}$ in the high energy limit. This value is generally consistent with GB conductances reported in the literature, which range from as low as $0.56\,\mathrm{GW\,m^{-2}\,K^{-1}}$ [14,26] or as high as $17.6\,\mathrm{GW\,m^{-2}\,K^{-1}}$ [27], depending on the GB and the material in question.

The inlay in Fig. 9(b) shows the conductance plotted as a function of the tilt angle with the structural groups differentiated by color. Note that the shape of the curve is similar to the inverted function $\gamma(\theta)$ shown in Fig. 5. This similarity highlights a strong correlation between the Kapitza conductance and the GB energy, which appears to be a rather general trend. This correlation was previously observed for GBs in Si [20,29], diamond-cubic carbon [27], silicon carbide [21], MgO [97], CeO_2 [98], Al_2O_3 [99], and other materials. Furthermore, a decrease of the GB conductance with the tilt angle was found for low-angle ($\theta < 30°$) tilt GBs in graphene [100,101], suggesting that this trend extends to 2D materials as well.

Figure 10(a) shows that the thermal GB width w follows a similar correlation with the GB energy as the thermal conductance. In particular, all w values break into three groups corresponding to the structural groups (Sec. IV A). In the high-energy limit, all three correlation lines converge to the same, universal width of about 0.25 nm, which is fittingly close to the interatomic distance. Knowing σ_K and w, the GB conductivity κ_K was evaluated from the relation $\kappa_K = \sigma_K w$. As expected, κ_K closely follows the same trends as σ_K and w, showing a strong correlation with the GB energy. It is interesting to note that, for the group 2 GBs (black symbols), σ_K decreases with GB energy while w increases. The two trends partially compensate each other, resulting in a relatively small slope (weaker dependence on the energy) for the conductivity correlation line. Each structural group follows its own correlation line, but all three lines converge to nearly

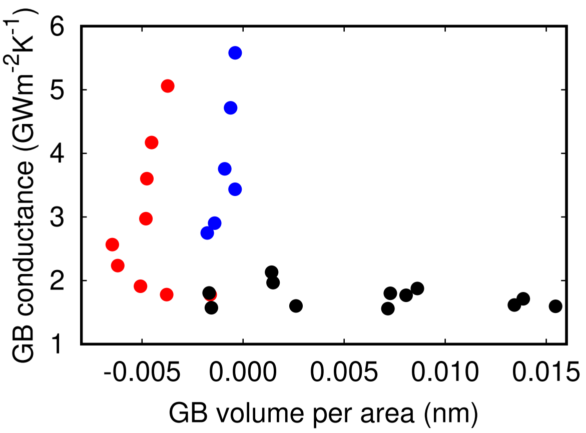

FIG. 11. GB conductance of Si GBs at 750 K plotted against the GB excess volume per unit GB area. The color of the points represents the structural groups as in Figs. 9 and 10.

the same, universal GB conductivity of about 0.4 W m^{-1} K^{-1} [Fig. 10(b)]. This value can be viewed as thermal conductivity of typical atomic structures existing in the cores of high-energy, high-angle GBs in Si.

The recent simulations of MgO GBs [97] revealed a strong correlation between the GB thermal conductance and the GB excess volume, while correlation with GB energy was much weaker. To compare these findings with the situation in Si, we have plotted the GB conductance at 750 K against the 0-K excess volume $[V]_N$ per the GB area. The excess volume is computed as $[V]_N = V - vN$, where V is the volume of a region with N atoms containing the GB and v is the volume per atom in an unperturbed reference grain. As illustrated in Fig. 11, the data points do separate into “clouds” corresponding to the structural groups. However, the slopes are either vertical or horizontal, which makes this correlation less informative than the correlation with energy. Figure 11 only serves to demonstrate the clustering behavior associated with the GB structural units rather than any meaningful statistical correlation. The preference for the GB conductance to correlate with the excess volume rather than energy is apparently a specific feature of the MgO GBs.

3. Temperature dependence

Six GBs were selected to examine the temperature dependence of the GB thermal conductance. Figure 12(a) reports the results for the (310) and (210) boundaries, which remain ordered up to high temperatures (cf. Fig. 8). In both boundaries, σ_K increases with temperature in more or less linear fashion. The trend for interface thermal conductance to slightly increase with temperature was observed in previous studies of GBs in Si and carbon [14,19,20,27,29,102], GBs in 2D graphene [100], and Si-Ge solid-solid interfaces [103]. For GBs, the likely reason is the existence of localized vibrational modes, which can exchange energy more easily as the anharmonicity increases at high temperatures.

The remaining four GBs exhibit the same trend at low temperatures [Fig. 12(b)] but deviate from this behavior at high temperatures. Namely, σ_K starts to *decrease* with temperature above about 1300 K. This change in the temperature dependence correlates with the onset of atomic disorder in these boundaries as was discussed in Sec. IV A (cf. Figs. 7 and 8). The effect can be explained by noting that the disordered GB structures begin to resemble a-Si, which is known to have a much lower thermal conductivity than ordered structures. A similar decrease was observed in simulations of the $\Sigma29$ 43.6° twist boundary in diamond carbon [27]. The observation of this effect in several GBs in Si suggests that the decrease in the GB conductance at premelting temperatures is a general trend common to most GBs in covalent materials.

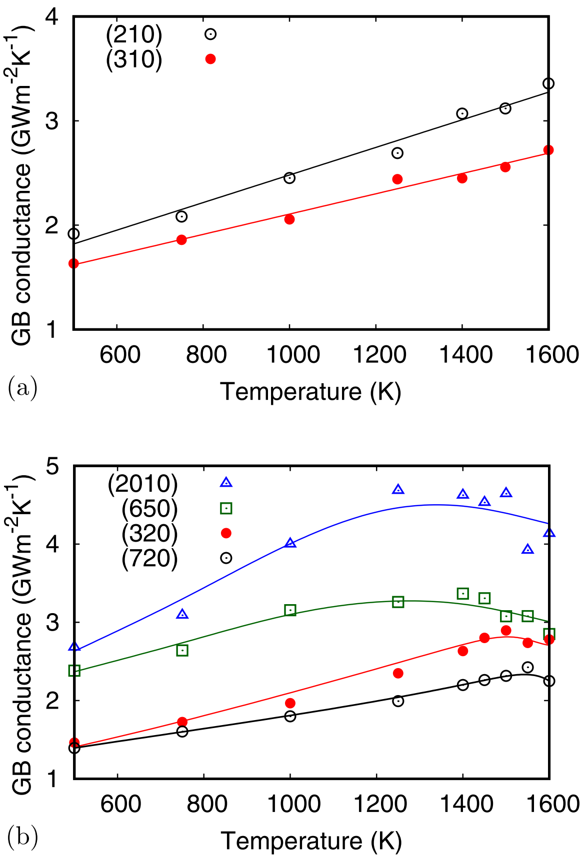

FIG. 12. The thermal conductance of GBs plotted as a function of temperature. (a) GBs remaining ordered up to the melting point. (b) GBs undergoing structural disordering at high temperatures. The lines are included as a guide to the eye.

To put these results in perspective, the temperature dependence of the GB conductivity κ_K was compared with that of the lattice conductivity κ. The latter was extracted from the linear portions of the temperature profiles during the NEMD simulations as discussed in Sec. III D. As a consistency check, κ was also computed by equilibrium MD simulations using the GK relation (Sec. III E). The GK method was also applied to compute κ of a-Si at several temperatures. The results are summarized in Fig. 13, where the low-angle (650) GB and the high-angle (210) GB have been chosen as representative cases. We find that the lattice conductivities obtained by the NEMD and GK methods are in good agreement with each other. The lattice conductivity rapidly decreases with temperature, following the $1/T$ relation predicted by the standard three-phonon scattering model [104]. In comparison, the GB conductivities increase with temperature very slowly

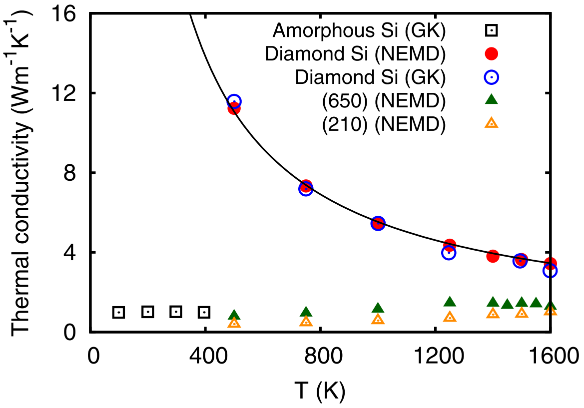

FIG. 13. Temperature dependence of thermal conductivity of c-Si (computed by two methods), a-Si, and two representative GBs. The line is a $1/T$ fit of the c-Si data.

and remain in the same ballpark as a-Si. The latter trend is consistent with the notion that the heat transport across GBs is likely to be dominated by localized vibrations rather than collective displacement waves as in the crystalline state. As a result, κ_K is not much different from that in the amorphous state. Both conductivities are expected to be close to the lower bond predicted by the Cahill-Pohl theory [105–107]. A rough estimate of this lower bound for Si, $0.4\ \mathrm{W\,m^{-1}\,K^{-1}}$, is provided by the high-energy extrapolation in Fig. 10(b).

C. Vibrational density of states

The vibrational DOS of GBs computed at different temperatures was compared with the DOS of the bulk Si phases in the effort to better understand the nature of the Kapitza resistance. As a reference point, Fig. 14 shows the DOS of c-Si computed with the present interatomic potential. The first, rather broad peak (band) represents the acoustic modes, whereas the sharp peak near the cutoff frequency originates from the optical branches. In the context of thermal conductivity, we are most interested in the acoustic modes. As temperature increases, the acoustic band shifts toward lower frequencies and becomes somewhat narrower and higher. The increased density of the medium-frequency acoustic phonons enhances their scattering rate, which is consistent with the observed decrease in thermal conductivity with temperature. The optical peak also initially shifts to lower frequencies, but this shift stops at higher temperatures.

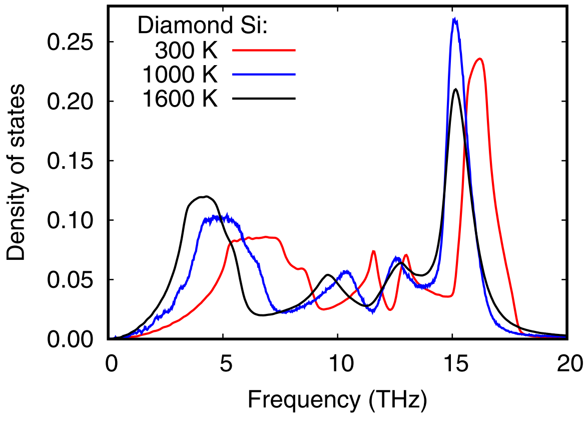

FIG. 14. Vibrational density of states for diamond silicon at several temperatures.

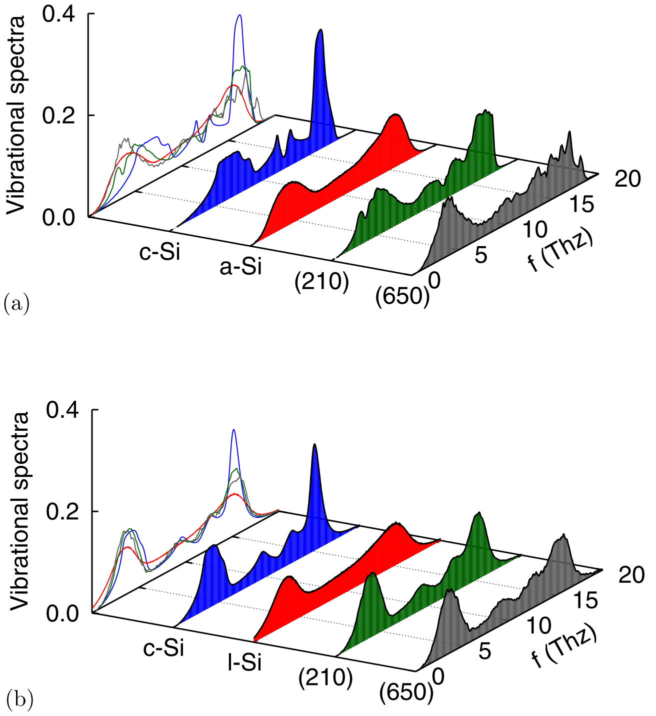

FIG. 15. Atomic vibrational spectra of (210) and (650) GBs in Si in comparison with DOS in c-Si, l-Si, and a-Si at (a) 300 K and (b) 1600 K.

Figure 15 displays the local DOS in the core regions of the (210) and (650) GBs in comparison with the DOS of c-Si and a-Si. Note that the a-Si DOS is qualitatively similar to the one seen experimentally by inelastic neutron scattering and in independent simulations [108–111]. At 300 K, the vibrational spectra of the (210) and (650) GBs tend to be intermediate in shape between the spectra of c-Si and a-Si. Similar to the amorphous structure, the acoustic band of both boundaries is shifted toward lower frequencies relative to c-Si. Furthermore, it additionally exhibits many localized peaks and looks more jagged than the a-Si DOS. In particular, the (210) GB DOS has a well-pronounced localized peak at about 3 THz. This peak suggests the existence of localized (nondispersive) vibrations in the GB core. Note that the frequency of this peak lies inside the acoustic frequency range that is most important for phonon scattering. As temperature increases to 1600 K, the 3-THz peak smooths out, as do other sharp peaks seen at 300 K. Except for the suppressed optical peak, the GB DOS becomes quite similar in shape to that of c-Si, and to some extent, to the a-Si DOS. This similarity is consistent with the convergence of thermal conductivities of the three structures at high temperatures. This convergence is illustrated in Fig. 13, where the c-Si thermal conductivity rapidly decreases with temperature while the GB conductivity slightly increases, so the two conductivities become close to each other.

More detailed information can be obtained by examining the vibrational spectra of individual GB sites. Figures 16 and

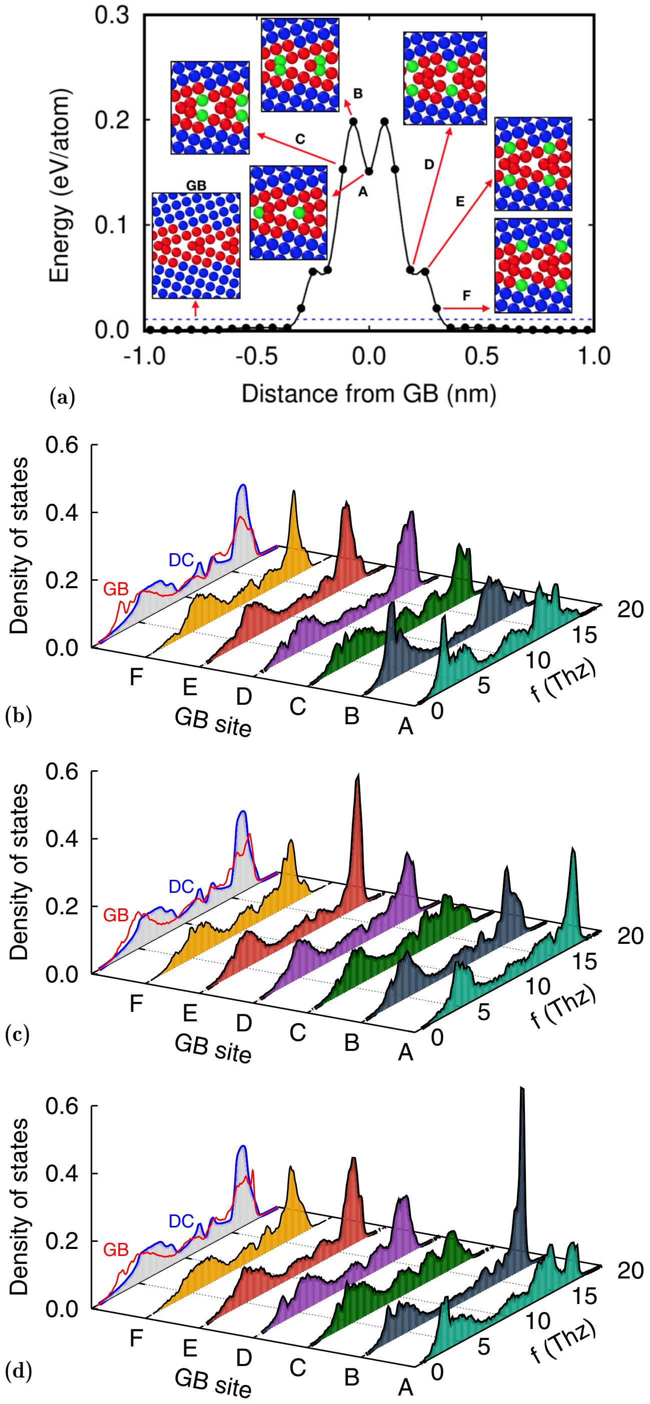

FIG. 16. (a) Selected atomic sites (shown in green and labeled A through F) in the (210) GB at 300 K. The sites are ranked according to the distance from the GB center and their energy is plotted as a function of this distance. The lines are drawn to highlight the trends. Panels (b), (c), and (d) show the vibrational density of states of the selected GB sites in the *x*, *y*, and *z* directions, respectively. The projection on the DOS-frequency plane shows the overall DOS of the GB core in the respective direction in comparison with that of diamond cubic (DC) Si.

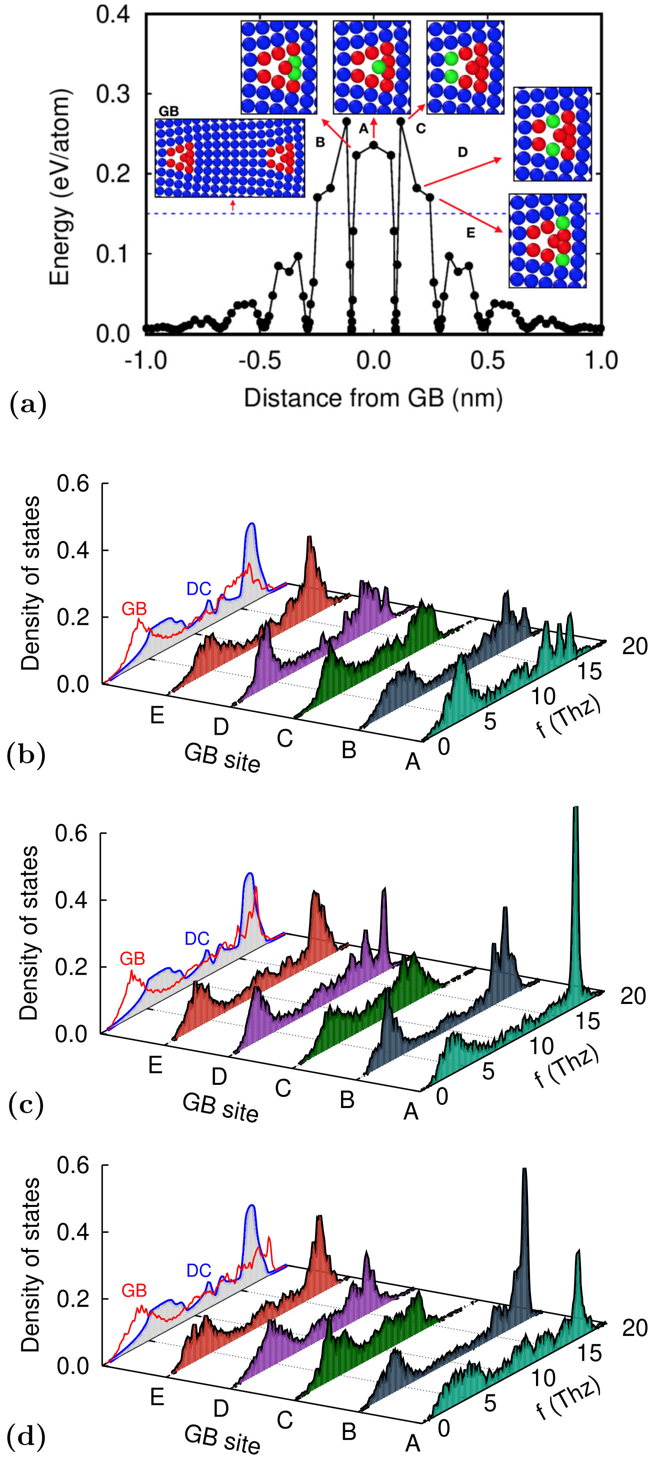

FIG. 17. (a) Selected atomic sites (shown in green and labeled A through F) in the (650) GB at 300 K. The sites are ranked according to the distance from the GB center and their energy is plotted as a function of this distance. The lines are drawn to highlight the trends. Panels (b), (c), and (d) show the vibrational density of states of the selected GB sites in the *x*, *y*, and *z* directions, respectively. The projection on the DOS-frequency plane shows the overall DOS of the GB core in the respective direction in comparison with that of diamond cubic (DC) Si.

17 show site-specific DOSs of the two GBs at 300 K resolved in the *x*, *y*, and *z* directions. The GB sites are labeled by letters A through F starting from the GB center and moving away in the *y* direction normal to the GB plane. The energies of the sites are indicated in the plot. The icons show a fragment

of the GB structure with the chosen atoms colored in green. Recall that whenever we show a GB structure, the x direction is horizontal, the y direction is vertical, and the z direction is normal to the page (parallel to the tilt axis).

In the (210) GB (Fig. 16), the 3-THz peak mentioned above features most prominently in vibrations along the x and z directions lying in the GB plane. This suggests that the peak is caused by localized in-plane vibrations. While this peak extends through two layers on ether side of the central layer A, it is highest for the vibrations of atom A sitting next to the open space existing at the center of the kite-shape structural unit. Thus, the localized vibrations occur by displacements of atom A toward this open space as well as parallel to the tilt axis. Another notable feature is that the acoustic band of the atoms B (located in the compressed region near the tip of the kite) is relatively narrow and is separated from the optical modes by a wide frequency range where the DOS is rather small. This frequency "gap" creates an acoustic mismatch between the vibrations of atoms B in the GB and the medium-frequency phonons in the lattice.

A similar frequency mismatch with lattice phonons exists for atoms B in the (650) GB (Fig. 17). Furthermore, a sharp peak occurs inside the acoustic band at about 5 THz for vibrations in all three directions. By contrast to the (210) GB, the atom A does not contribute much to this peak. Instead, the 5-THz peak is largely caused by vibrations of atoms B in the y direction. Another sharp peak at about 5 THz is produced by vibrations of atoms C in the z direction. Since atoms B and C are spatially separated from each other and have different local environments (relatively open and compressed, respectively), these two peaks represent different local modes and their frequency match is likely to be coincidental.

The Supplemental Material [74] presents the results of similar site-specific DOS calculations at 1600 K. Some of the features mentioned above can still be discerned, but in general the spectra look much smoother. The local peaks within the acoustic band are barely noticeable, but atoms B still exhibit a wide "gap" separating the acoustic and optical bands and thus creating a mismatch with the acoustic phonons in the lattice.

V. SUMMARY AND CONCLUSIONS

We have conducted a systematic study of thermal (Kapitza) resistance of GBs in Si, focusing on a set of [001] symmetrical tilt GBs spanning the entire misorientation range. The simulations are based on classical MD and utilize a recently developed interatomic potential [33]. Careful equilibration of the GBs ensured that their structures are representative of the equilibrium GBs occurring under experimental conditions. The thermal conductance of the GBs was determined by the NEMD method (also known as the direct method) over a wide range of temperatures. In this method, the GB conductance is extracted from the temperature jump across the GB measured in the presence of heat flux normal to the boundary (Fig. 1). The method also yields the GB thermal width, which can be used to find the effective GB conductivity from the GB conductance. For comparison, thermal conductivity of bulk Si phases (crystalline, amorphous, and liquid) was computed by equilibrium MD simulations using the GK method.

Two limitations of our methodology should be mentioned. First, we rely on a classical interatomic potential [33]. While this potential presents a significant improvement over the popular potentials such as SW [32] and T89 [75], we find that it underestimates the lattice thermal conductivity of c-Si with respect to those potentials, as well as experimental data and first-principles calculations. On the other hand, the tests reported in this paper show the GB conductance and the thermal conductivity of a-Si predicted by this potential are very similar values to those obtained with other potentials. Given that the present potential is likely to be more reliable for the modeling of defect structures such as GBs [33], we consider it a reasonable choice for this study. The second limitation is that the classical MD simulations are not expected to accurately represent the actual behavior of the thermal conductivity at low temperatures dominated by quantum effects. Given that many of the results reported here refer to temperatures below the experimental Debye temperature of c-Si, we only expect that they capture the main qualitative trends of the GB structure-conductivity relationships.

One of the main results of this work is the established correlation between the GB excess energy and the GB thermal resistance. Specifically, all GBs studied here naturally break into three groups according to the type of elementary structural units forming their core (Fig. 5). Within each group, the GB conductivity strongly correlates with the GB energy (Figs. 9 and 10). While the correlation relations are different within each group, the remarkable fact is that all three correlations predict the same upper bound of the thermal conductivity achieved in the high-energy limit. This limiting values is close to thermal conductivity of a-Si, suggesting that the heat transport mechanisms are similar. In fact, the GB and a-Si conductivities remain in the same ballpark at all temperatures (Fig. 13).

While the lattice thermal conductivity decreases with increasing temperature, the GB conductivity slightly increases. The latter effect can be explained by the enhanced energy transfer between the localized vibrational modes in the GB core as the anharmonicity of vibrations increases with temperature. In some of the GBs, however, this trend reverses and the conductivity starts decreasing at high temperatures [Fig. 8(b)]. It has been shown that this effect is caused by structural disordering of such GBs when approaching the melting temperature (premelting phenomenon, Fig. 7).

To gain a better microscopic understanding of the Kapitza resistance, we have analyzed the vibrational spectra of the GBs extracted from the velocity autocorrelation function. Using this method, the vibrational DOS can be computed specifically for atoms located within the GB core region, or even for individual atoms. Furthermore, the DOS can be resolved along the three Cartesian axes. Such directional vibrational spectra carry valuable information about the atomic vibrations parallel and normal to the tilt axis as well as in the direction normal to the GB plane. One of the important findings is the existence of sharp peaks in the acoustic frequency range of the vibrational spectra (Figs. 15, 16, and 17). Such peaks are usually caused by nonpropagating modes, such as resonances and Einstein-like localized vibrations. The origin of these peaks has been traced back to the strong inhomogeneity of the atomic environments featured by the GB core, including alternating regions of tension and compression. The tensile environments exist in relatively open locations near the centers of the structural units. Atoms in such environments are loosely bound and vibrate anharmonically, especially at high temperatures. This behavior is somewhat reminiscent of the "rattling" of caged atoms in phonon-glass systems [112]. One more prominent feature is the existence of low-density regions ("gaps") between the acoustic and optical bands in the spectra of some GB atoms (Figs. 16 and 17). Such "gaps" give rise to a mismatch with the medium-frequency lattice phonons, which are important for thermal conductivity.

Further progress in the understanding of Kapitza resistance can be made by specifically analyzing the atomic displacements in the normal modes of a bicrystal containing a GB, as was recently done for a model system composed of two lattice-mismatching Lennard-Jones solids [15]. This analysis should permit separation of the lattice modes from the modes localized in the GB core, and among the latter, identification of the local modes and resonances. The relaxation times of individual modes in the GB region can also be computed, along with other measures anharmonicity and localization, and the results can be correlated with the local structural environments. Improving the accuracy of the interatomic potential is another important task for the future. One possible path toward this goal is utilizing one of the machine-learning potentials, such as the physically informed neural network potential proposed in Ref. [113]. Such potential prove access to large-scale simulations while predicting the energies of atomic configurations on a nearly first-principles level.

ACKNOWLEDGMENTS

This research was performed while J.H. was supported by an NRC Research Associateship award at the National Institute of Standards and Technology (NIST). The work at George Mason University was supported by the US Department of Energy, Office of Basic Energy Sciences, Division of Materials Sciences and Engineering, the Physical Behavior of Materials Program, through Grant No. DE-FG02-01ER45871.

---

[1] D. G. Cahill, W. K. Ford, K. E. Goodson, G. D. Mahan, A. Majumdar, H. J. Maris, R. Merlin, and S. R. Phillpot, Nanoscale thermal transport, J. Appl. Phys. **93**, 793 (2003).

[2] P. K. Schelling, L. Shi, and K. E. Goodson, Managing heat for electronics, Mater. Today **8**, 30 (2005).

[3] M. S. Dresselhaus, G. Chen, M. Y. Tang, R. Yang, H. Lee, D. Wang, Z. Ren, J. P. Fleurial, and P. Gogna, New directions for low-dimensional thermoelectric materials, Adv. Mater. **19**, 1043 (2007).

[4] A. J. Minnich, M. S. Dresselhaus, Z. F. Ren, and G. Chen, Bulk nanostructured thermoelectric materials: Current research and future prospects, Energy Environ. Sci. **2**, 466 (2009).

[5] E. S. Toberer, A. Zevalkink, and G. J. Snyder, Phonon engineering through crystal chemistry, J. Mater. Chem. **21**, 15843 (2011).

[6] M. Zebarjadi, K. Esfarjani, M. S. Dresselhaus, Z. F. Ren, and G. Chen, Perspectives on thermoelectrics: From fundamentals to device applications, Energy Environ. Sci. **5**, 5147 (2012).

[7] X. Zhang, M. Hu, K. P. Giapis, and D. Poulikakos, Schemes for and mechanisms of reduction in thermal conductivity in nanostructured thermoelectrics, J. Heat Transfer **134**, 102402 (2012).

[8] D. G. Cahill, P. V. Braun, G. Chen, D. R. Clarke, S. Fan, K. E. Goodson, P. Keblinski, W. P. King, G. D. Mahan, A. Majumdar, H. J. Maris, S. R. Phillpot, E. Pop, and L. Shi, Nanoscale thermal transport. II. 2003–2012, Appl. Phys. Rev. **1**, 011305 (2014).

[9] E. T. Swartz and R. O. Pohl, Thermal boundary resistance, Rev. Mod. Phys. **61**, 605 (1989).

[10] X. Wang, H. Lee, Y. Lan, G. Zhu, G. Joshi, D. Wang, J. Yang, A. Muto, M. Tang, J. Klatsky, S. Song, M. Dresselhaus, G. Chen, and Z. Ren, Enhanced thermoelectric figure of merit in nanostructured n-type silicon germanium bulk alloy, Appl. Phys. Lett. **93**, 193121 (2008).

[11] G. H. Zhu, H. Lee, Y. C. Lan, X. W. Wang, G. Joshi, D. Z. Wang, J. Yang, D. Vashaee, H. Guilbert, A. Pillitteri, M. S. Dresselhaus, G. Chen, and Z. F. Ren, Increased Phonon Scattering by Nanograins and Point Defects in Nanostructured Silicon with a Low Concentration of Germanium, Phys. Rev. Lett. **102**, 196803 (2009).

[12] Q. Hao, G. Zhu, G. Joshi, X. Wang, A. Minnich, Z. Ren, and G. Chen, Theoretical studies on the thermoelectric figure of merit of nanograined bulk silicon, Appl. Phys. Lett. **97**, 063109 (2010).

[13] I. M. Khalatnikov, *Introduction to the Theory of Superfluidity* (W. A. Benjamin, New York, 1965).

[14] P. K. Schelling, Kapitza conductance and phonon scattering at grain boundaries by simulation, J. Appl. Phys. **95**, 6082 (2004).

[15] K. Gordiz and A. Henry, Phonon transport at interfaces: Determining the correct modes of vibration, J. Appl. Phys. **119**, 015101 (2016).

[16] A. Chernatynskiy and S. R. Phillpot, Evaluation of computational techniques for solving the Boltzmann transport equation for lattice thermal conductivity calculations, Phys. Rev. B **82**, 134301 (2010).

[17] C. W. Nan and R. Birringer, Determining the Kapitza resistance and the thermal conductivity of polycrystals: A simple model, Phys. Rev. B **57**, 8264 (1998).

[18] A. Maiti, G. D. Mahan, and S. T. Pantelides, Dynamical simulations of nonequilibrium processes: Heat flow and the Kapitza resistance across grain boundaries, Solid State Commun. **102**, 517 (1997).

[19] S. H. Ju and X. G. Liang, Investigation on interfacial thermal resistance and phonon scattering at twist boundary of silicon, J. Appl. Phys. **113**, 053513 (2013).

[20] C. Kimmer, S. Aubry, A. Skye, and P. K. Schelling, Scattering of phonons from a high-energy grain boundary in silicon: Dependence on angle of incidence, Phys. Rev. B **75**, 144105 (2007).

[21] J. P. Crocombette and L. Gelebart, Multiscale modeling of the thermal conductivity of polycrystalline silicon carbide, J. Appl. Phys. **106**, 083520 (2009).

[22] X. Chen, W. Li, L. Xiong, Y. Li, S. Yang, Z. Zheng, D. L. McDowell, and Y. Chen, Ballistic-diffusive phonon heat transport across grain boundaries, Acta Mater. **136**, 355 (2017).

[23] X. Chen, L. Xiong, A. Chernatynskiy, and Y. Chen, A molecular dynamics study of tilt grain boundary resistance to slip and heat transfer in nanocrystalline silicon, J. Appl. Phys. **116**, 244309 (2014).

[24] N. Goel, E. B. Webb III, A. Oztekin, J. M. Rickman, and S. Neti, Kapitza resistance at segregated boundaries in β-SiC, J. Appl. Phys. **118**, 115101 (2015).

[25] A. Bodapati, P. K. Schelling, S. R. Phillpot, and P. Keblinski, Vibrations and thermal transport in nanocrystalline silicon, Phys. Rev. B **74**, 245207 (2006).

[26] Q. Tang and Y. Yao, The Kapitza resistance across grain boundary by molecular dynamics simulation, Nanoscale Microscale Thermophys. Eng. **10**, 387 (2006).

[27] T. Watanabe, B. Ni, and S. R. Phillpot, Thermal conductance across grain boundaries in diamond from molecular dynamics simulation, J. Appl. Phys. **102**, 063503 (2007).

[28] A. Bodapati, P. Keblinski, P. K. Schelling, and S. R. Phillpot, Crossover in thermal transport mechanism in nanocrystalline silicon, Appl. Phys. Lett. **88**, 141908 (2006).

[29] S. Aubry, C. J. Kimmer, A. Skye, and P. K. Schelling, Comparison of theoretical and simulation-based predictions of grain-boundary Kapitza conductance in silicon, Phys. Rev. B **78**, 064112 (2008).

[30] N. Goel, E. Webb III, J. Rickman, A. Oztekin, and S. Neti, Thermal transport across symmetric tilt grain boundaries in β-SiC: Effect of dopants and temperature, AIP Adv. **6**, 075101 (2016).

[31] A. P. Sutton, and R. W. Balluffi, *Interfaces in Crystalline Materials* (Clarendon Press, Oxford, UK, 1995).

[32] F. H. Stillinger and T. A. Weber, Computer simulation of local order in condensed phases of silicon, Phys. Rev. B **31**, 5262 (1985).

[33] G. P. Purja Pun and Y. Mishin, Optimized interatomic potential for silicon and its application to thermal stability of silicene, Phys. Rev. B **95**, 224103 (2017).

[34] Y. Lysogorskiy, T. Hammerschmidt, J. Janssen, J. Neugebauer, and R. Drautz, Transferability of interatomic potentials for molybdenum and silicon, Modell. Simul. Mater. Sci. Eng. **27**, 025007 (2019).

[35] Y. H. Lee, R. Biswas, C. M. Soukoulis, C. Z. Wang, C. T. Chan, and K. M. Ho, Molecular-dynamics simulation of thermal conductivity in amorphous silicon, Phys. Rev. B **43**, 6573 (1991).

[36] S. G. Volz and G. Chen, Molecular-dynamics simulation of thermal conductivity of silicon crystals, Phys. Rev. B **61**, 2651 (2000).

[37] P. K. Schelling, S. R. Phillpot, and P. Keblinski, Comparison of atomic-level simulation methods for computing thermal conductivity, Phys. Rev. B **65**, 144306 (2002).

[38] A. S. Henry and G. Chen, Spectral phonon transport properties of silicon based on molecular dynamics simulations and lattice dynamics, Comp. Theor. Nanoscience **5**, 1 (2008).

[39] Y. He, I. Savic, D. Donadiob, and G. Galli, Lattice thermal conductivity of semiconducting bulk materials: Atomistic simulations, Phys. Chem. Chem. Phys. **14**, 16209 (2012).

[40] E. Lampin, P. L. Palla, P. A. Francioso, and F. Cleri, Thermal conductivity from approach-to-equilibrium molecular dynamics, J. Appl. Phys. **114**, 033525 (2013).

[41] M. Puligheddu, F. Gygi, and G. Galli, First-principles simulations of heat transport, Phys. Rev. Mater. **1**, 060802 (2017).

[42] R. Kubo, The fluctuation-dissipation theorem, Rep. Prog. Phys. **29**, 255 (1966).

[43] R. Kubo, M. Toda, and N. Hashitsume, *Statistical Physics II: Nonequilibrium Statistical Mechanics*, 2nd ed., Solid-State Sciences Vol. 31 (Springer-Verlag, Berlin, 1991).

[44] H. B. Callen and T. A. Welton, Irreversibility and generalized noise, Phys. Rev. **83**, 34 (1951).

[45] J. M. Ziman, *Electrons and Phonons: The Theory of Transport Phenomena in Solids*, Oxford Texts in the Physical Sciences (Oxford University Press, Oxford, UK, 1960).

[46] J. Tersoff, New empirical approach for the structure and energy of covalent systems, Phys. Rev. B **37**, 6991 (1988).

[47] J. Tersoff, Empirical interatomic potential for silicon with improved elastic properties, Phys. Rev. B **38**, 9902 (1988).

[48] M. Z. Bazant, E. Kaxiras, and J. F. Justo, Environment-dependent interatomic potential for silicon, Phys. Rev. B **56**, 8542 (1997).

[49] J. Garg, N. Bonini, B. Kozinsky, and N. Marzari, Role of Disorder and Anharmonicity in the Thermal Conductivity of Silicon-Germanium Alloys: A First-Principles Study, Phys. Rev. Lett. **106**, 045901 (2011).

[50] F. Zhou, W. Nielson, Y. Xia, and V. Ozoliņš, Lattice Anharmonicity and Thermal Conductivity from Compressive Sensing of First-Principles Calculations, Phys. Rev. Lett. **113**, 185501 (2014).

[51] J. Garg, N. Bononi, and N. Marzari, First-principles determination of phonon lifetimes, mean free paths, and thermal conductivities in crystalline materials: Pure silicon and germanium, in *Length-Scale Dependent Phonon Interactions*, Topics in Applied Physics Vol. 128, edited by S. L. Shindé and G. P. Srivastava (Springer-Verlag, Heidelberg, Germany 2014), pp. 115–136.

[52] A. Marcolongo, P. Umari, and S. Baroni, Microscopic theory and quantum simulation of atomic heat transport, Nat. Phys. **12**, 80 (2016).

[53] P. L. Kapitza, The study of heat transfer in helium II, J. Phys. (USSR) **4**, 181 (1941).

[54] P. L. Kapitza, Heat transfer and superfluidity of helium II, Phys. Rev. **60**, 354 (1941).

[55] X. Chen, A. Chernatynskiy, L. Xiong, and Y. Chen, A coherent phonon pulse model for transient phonon thermal transport, Comput. Phys. Commun. **195**, 112 (2015).

[56] X. Chen, W. Li, A. DIaz, Y. Li, Y. Chen, and D. L. McDowell, Recent progress in the concurrent atomistic-continuum method and its applications in phonon transport, MRS Commun. **7**, 785 (2017).

[57] Y. Li, W. Li, X. Chen, A. Diaz, D. L. McDowell, and Y. Chen, Phonon spectrum and phonon focusing in coarse-grained atomistic simulations, Comput. Mater. Sci. **162**, 21 (2019).

[58] S. Plimpton, Fast parallel algorithms for short-range molecular-dynamics, J. Comput. Phys. **117**, 1 (1995).

[59] A. Stukowski, Visualization and analysis of atomistic simulation data with OVITO, the open visualization tool, Modell. Simul. Mater. Sci. Eng. **18**, 015012 (2010).

[60] S. von Alfthan, K. Kaski, and A. P. Sutton, Order and structural units in simulations of twist grain boundaries in silicon at absolute zero, Phys. Rev. B **74**, 134101 (2006).

[61] S. von Alfthan, P. D. Haynes, K. Kaski, and A. P. Sutton, Are the Structures of Twist Grain Boundaries in Silicon Ordered at 0 K?, Phys. Rev. Lett. **96**, 055505 (2006).

[62] T. Frolov, D. L. Olmsted, M. Asta, and Y. Mishin, Structural phase transformations in metallic grain boundaries, Nat. Commun. **4**, 1899 (2013).

[63] T. Frolov, S. V. Divinski, M. Asta, and Y. Mishin, Effect of Interface Phase Transformations on Diffusion and Segregation in High-Angle Grain Boundaries, Phys. Rev. Lett. **110**, 255502 (2013).

[64] T. Frolov, M. Asta, and Y. Mishin, Segregation-induced phase transformations in grain boundaries, Phys. Rev. B **92**, 020103(R) (2015).

[65] J. Han, V. Vitek, and D. J. Srolovitz, Grain-boundary metastability and its statistical properties, Acta Mater. **104**, 259 (2016).

[66] J. Hickman and Y. Mishin, Extra variable in grain boundary description, Phys. Rev. Mater. **1**, 010601 (2017).

[67] P. J. Steinhardt, D. R. Nelson, and M. Ronchetti, Bond-orientational order in liquids and glasses, Phys. Rev. B **28**, 784 (1983).

[68] P. Jund and R. Jullien, Molecular-dynamics calculation of the thermal conductivity of vitreous silica, Phys. Rev. B **59**, 13707 (1999).

[69] F. Müller-Plathe, A simple nonequilibrium molecular dynamics method for calculating the thermal conductivity, J. Chem. Phys. **106**, 6082 (1997).

[70] J. Hickman and Y. Mishin, Temperature fluctuations in canonical systems: Insights from molecular dynamics simulations, Phys. Rev. B **94**, 184311 (2016).

[71] Y. Mishin and J. Hickman, Energy spectrum of a Langevin oscillator, Phys. Rev. E **94**, 062151 (2016).

[72] P. C. Howell, Comparison of molecular dynamics methods and interatomic potentials for calculating the thermal conductivity of silicon, J. Chem. Phys. **137**, 224111 (2012).

[73] M. E. Khaled, L. Zhang, and W. Liu, Some critical issues in the characterization of nanoscale thermal conductivity by molecular dynamics analysis some critical issues in the characterization of nanoscale thermal conductivity by molecular dynamics analysis, Modell. Simul. Mater. Sci. Eng. **26**, 055002 (2018).

[74] See Supplemental Material at http://link.aps.org/supplemental/10.1103/PhysRevMaterials.4.033405 for convergence test results and complete set of GB energy plots and GB structures.

[75] J. Tersoff, Modeling solid-state chemistry: Interatomic potentials for multicomponent systems, Phys. Rev. B **39**, 5566 (1989).

[76] T. Kumagai, S. Izumi, S. Hara, and S. Sakai, Development of bond-order potentials that can reproduce the elastic constants and melting point of silicon for classical molecular dynamics simulation, Comput. Mater. Sci. **39**, 457 (2007).

[77] R. K. Kremer, K. Graf, M. Cardona, G. G. Devyatykh, A. V. Gusev, A. M. Gibin, A. V. Inyushkin, A. N. Taldenkov, and H. J. Pohl, Thermal conductivity of isotopically enriched ^{28}Si: revisited, Solid State Commun. **131**, 499 (2004).

[78] H. Wada and T. Kamijoh, Thermal conductivity of amorphous silicon, Jpn. J. Appl. Phys. **35**, L648 (1996).

[79] J. L. Braun, C. H. Baker, A. Giri, M. Elahi, K. Artyushkova, T. E. Beechem, P. M. Norris, Z. C. Leseman, J. T. Gaskins, and P. E. Hopkins, Size effects on the thermal conductivity of amorphous silicon thin films, Phys. Rev. B **93**, 140201(R) (2016).

[80] H. Kobatake, H. Fukuyama, and I. Minato, Noncontact measurement of thermal conductivity of liquid silicon in a static magnetic field, Appl. Phys. Lett. **90**, 094102 (2007).

[81] S. R. Grest, G. S. Nagel, A. Rahman, and T. A. Witten Jr., Density of states and the velocity autocorrelation function derived from quench studies, J. Chem. Phys. **74**, 3532 (1981).

[82] L. T. Kong, Phonon dispersion measured directly from molecular dynamics simulations, Comput. Phys. Commun. **182**, 2201 (2011).

[83] W. T. Read and W. Shockley, Dislocation models of crystal grain boundaries, Phys. Rev. **78**, 275 (1950).

[84] J. Zhang, C. Z. Wang, and K. M. Ho, Finding the low-energy structures of Si [001] symmetric tilted grain boundaries with a genetic algorithm, Phys. Rev. B **80**, 174102 (2009).

[85] O. A. Shenderova, D. W. Brenner, and L. H. Yang, Atomistic simulations of structures and mechanical properties of polycrystalline diamond: Symmetrical $\langle 001 \rangle$ tilt grain boundaries, Phys. Rev. B **60**, 7043 (1999).

[86] A. A. Levi, D. Smith, and J. T. Wetzel, Calculated structures for [001] symmetrical tilt grain boundaries in silicon, J. Appl. Phys. **69**, 2048 (1991).

[87] S. Bringuier, V. R. Manga, K. Runge, P. Deymier, and K. Muralidharan, An atomic scale characterization of coupled grain boundary motion in silicon bicrystals, Philos. Mag. **95**, 4118 (2015).

[88] J. R. Morris, Z. Y. Lu, D. M. Ring, J. B. Xiang, K. M. Ho, C. Z. Wang, and C. L. Fu, First-principles determination of the $\Sigma = 13\{510\}$ symmetric tilt boundary structure in silicon and germanium, Phys. Rev. B **58**, 11241 (1998).

[89] J. L. Rouviere and A. Bourret, Analysis of structures of symmetrical [001] tilt grain boundaries in silicon and germanium, J. Phys. Colloq. **51**, C1-329 (1990).

[90] A. Bourret, J. L. Rouviere, and J. M. Penisson, Structure determination of planar defects in crystals of germanium and molybdenum by HREM, Acta Crystallogr. Sect. A **44**, 838 (1988).

[91] J. Hickman and Y. Mishin, Disjoining potential and grain boundary premelting in binary alloys, Phys. Rev. B **93**, 224108 (2016).

[92] Y. Mishin, W. J. Boettinger, J. A. Warren, and G. B. McFadden, Thermodynamics of grain boundary premelting in alloys. I. Phase field modeling, Acta Mater. **57**, 3771 (2009).

[93] S. J. Fensin, D. Olmsted, D. Buta, M. Asta, A. Karma, and J. J. Hoyt, Structural disjoining potential for grain-boundary premelting and grain coalescence from molecular-dynamics simulations, Phys. Rev. E **81**, 031601 (2010).

[94] O. H. Duparc and M. Torrent, A candidate for grain boundary pipe diffusion and intrinsic electrical activity in silicon, Mater. Sci. Forum **207–209**, 221 (1996).

[95] S. von Alfthan, K. Kaski, and A. P. Sutton, Molecular dynamics simulations of temperature-induced structural transitions at twist boundaries in silicon, Phys. Rev. B **76**, 245317 (2007).

[96] M. G. Holland, Analysis of lattice thermal conductivity, Phys. Rev. **132**, 2461 (1963).

[97] S. Fujii, T. Yokoi, and M. Yoshiya, Atomistic mechanisms of thermal transport across symmetric tilt grain boundaries in MgO, Acta Mater. **171**, 154 (2019).

[98] A. Chernatynskiy, X. M. Bai, and J. Gan, Systematic investigation of the misorientation- and temperature-dependent Kapitza resistance in CeO_2, Int. J. Heat Mass Transf. **99**, 461 (2016).

[99] K. Tai, A. Lawrence, M. P. Harmer, and S. J. Dillon, Misorientation dependence of Al_2O_3 grain boundary thermal resistance, Appl. Phys. Lett. **102**, 034101 (2013).

[100] A. Cao and J. Qu, Kapitza conductance of symmetric tilt grain boundaries in graphene, J. Appl. Phys. **111**, 053529 (2012).

[101] A. Bagri, S. P. Kim, R. S. Ruoff, and V. B. Shenoy, Thermal transport across twin grain boundaries in polycrystalline graphene from nonequilibrium molecular dynamics simulations, Nano Lett. **11**, 3917 (2011).

[102] X. H. Chen, L. Lu, and K. Lu, Grain size dependence of tensile properties in ultrafine-grained Cu with nanoscale twins, Scr. Mater. **64**, 311 (2011).

[103] E. S. Landry and A. J. H. McGaughey, Thermal boundary resistance predictions from molecular dynamics simulations and theoretical, Phys. Rev. B **80**, 165304 (2009).

[104] C. Kittel, *Introduction to Sold State Physics* (Wiley-Interscience, New York, 1986).

[105] D. G. Cahill and R. O. Pohl, Heat flow and lattice vibrations in glasses, Solid State Commun. **70**, 927 (1989).

[106] D. G. Cahill, S. K. Watson, and R. O. Pohl, Lower limit to the thermal conductivity of disordered crystals, Phys. Rev. B **46**, 6131 (1992).

[107] R. O. Pohl, Lattice vibrations in glasses, J. Non-Cryst. Solids **352**, 3363 (2006).

[108] W. A. Kamitakahara, H. R. Shanks, J. F. McClelland, U. Buchenau, F. Gompf, and L. Pintschovius, Measurement of Phonon Densities of States for Pure and Hydrogenated Amorphous Silicon, Phys. Rev. Lett. **52**, 644 (1984).

[109] R. Car and M. Parrinello, Structural, Dymanical, and Electronic Properties of Amorphous Silicon: An *ab initio* Molecular-Dynamics Study, Phys. Rev. Lett. **60**, 204 (1988).

[110] R. Biswas, A. M. Bouchard, W. A. Kamitakahara, G. S. Grest, and C. M. Soukoulis, Vibrational Localization in Amorphous Silicon, Phys. Rev. Lett. **60**, 2280 (1988).

[111] J. L. Feldman, M. D. Kluge, P. B. Allen, and F. Wooten, Thermal conductivity and localization in glasses: Numerical study of a model of amorphous silicon, Phys. Rev. B **48**, 12589 (1993).

[112] T. Takabatake, K. Suekuni, T. Nakayama, and E. Kaneshita, Phonon-glass electron-crystal thermoelectric clathrates: Experiments and theory, Rev. Mod. Phys. **86**, 669 (2014).

[113] G. P. Purja Pun, R. Batra, R. Ramprasad, and Y. Mishin, Physically informed artificial neural networks for atomistic modeling of materials, Nat. Commun. **10**, 2339 (2019).